# Secondary ice production processes in wintertime alpine mixed-phase clouds

Paraskevi Georgakaki[1], Georgia Sotiropoulou[1,2,5], Étienne Vignon[3], Anne-Claire Billault-Roux[4], Alexis Berne[4] and Athanasios Nenes[1,5]

[1]Laboratory of Atmospheric Processes and their Impacts, School of Architecture, Civil & Environmental Engineering, École Polytechnique Fédérale de Lausanne, Lausanne, CH-1015, Switzerland
[2]Department of Meteorology, Stockholm University & Bolin Center for Climate Research, Stockholm, Sweden
[3]Laboratoire de Météorologie Dynamique/IPSL/Sorbone Université/CNRS, UMR 8539, Paris, France
[4]Environmental Remote Sensing Laboratory, School of Architecture, Civil & Environmental Engineering, École Polytechnique Fédérale de Lausanne, Lausanne, CH-1015, Switzerland
[5]Center for Studies of Air Quality and Climate Change, Institute of Chemical Engineering Sciences, Foundation for Research and Technology Hellas, Patras, GR-26504, Greece

*Correspondence to*: athanasios.nenes@epfl.ch

## Abstract

Observations of orographic mixed-phase clouds (MPCs) have long shown that measured ice crystal number concentrations (ICNCs) can exceed the concentration of ice nucleating particles by orders of magnitude. Additionally, model simulations of alpine clouds are frequently found to underestimate the amount of ice compared with observations. Surface-based blowing snow, hoar frost and secondary ice production processes have been suggested as potential causes, but their relative importance and persistence remains highly uncertain. Here we study ice production mechanisms in wintertime orographic MPCs observed during the Cloud and Aerosol Characterization Experiment (CLACE) 2014 campaign at the Jungfraujoch site in the Swiss Alps with the Weather Research and Forecasting model (WRF). Simulations suggest that droplet shattering is not a significant source of ice crystals at this specific location – but break-up upon collisions between ice particles is quite active, elevating the predicted ICNCs by up to 3 orders of magnitude, which is consistent with observations. The initiation of the ice-ice collisional break-up mechanism is primarily associated with the occurrence of seeder-feeder events from higher precipitating cloud layers. The enhanced aggregation of snowflakes is found to drive secondary ice formation in the simulated clouds, the role of which is strengthened when the large hydrometeors interact with the primary ice crystals formed in the feeder cloud. Including a constant source of cloud ice crystals from blowing snow, through the action of the break-up mechanism, can episodically enhance ICNCs. Increases in secondary ice fragment generation can be counterbalanced by enhanced orographic precipitation, which seems to prevent explosive multiplication and cloud dissipation. These findings highlight the importance of secondary ice and "seeding" mechanisms – primarily falling ice from above and to a lesser

39    degree blowing ice from the surface – which frequently enhance primary ice and determine the
40    phase state and properties of MPCs.

## 1.   Introduction

43    Understanding orographic precipitation is one of the most critical aspects of weather
44    forecasting in mountainous regions (Roe, 2005; Rotunno and Houze, 2007; Chow et al., 2013).
45    Orographic clouds are often mixed-phase clouds (MPCs), containing simultaneously
46    supercooled liquid water droplets and ice crystals (Lloyd et al., 2015; Lohmann et al., 2016;
47    Henneberg et al., 2017). MPCs are persistent in complex mountainous terrain, because the high
48    updraft velocity conditions generate supercooled liquid droplets faster than can be depleted by
49    ice production mechanisms (Korolev and Isaac, 2003; Lohmann et al., 2016). In mid- and high-
50    latitude environments almost all precipitation originates from the ice phase (Field and
51    Heymsfield, 2015; Mülmenstädt et al., 2015), emphasizing the necessity of correctly
52    simulating the amount and distribution of both liquid water and ice (i.e., the liquid-ice phase
53    partitioning) in MPCs (Korolev et al., 2017).
54         Our understanding of MPCs remains incomplete owing to the numerous and highly
55    nonlinear cloud microphysical pathways driving their properties and evolution (Morrison et al.,
56    2012). MPCs tend to glaciate over time through the Wegener-Bergeron-Findeisen (WBF)
57    process, which is the rapid ice crystal growth at the expense of the surrounding evaporating
58    cloud droplets (Bergeron, 1935; Findeisen, 1938). Ice crystals falling from a high-level seeder
59    cloud into a lower-level cloud (external "seeder-feeder" event) or a lower-lying part of the
60    same cloud (in-cloud "seeder-feeder" event) can trigger cloud glaciation and enhance
61    precipitation over mountains (e.g., Roe, 2005, Reinking et al., 2000; Purdy et al., 2005; Mott
62    et al., 2014; Ramelli et al., 2021). Analysis of satellite remote sensing over the 11-year period
63    between April 2006 and October 2017 suggest that seeding events are widespread over
64    Switzerland, occurring with a frequency of 31% of the total observations in which cirrus clouds
65    seed lower mixed-phase cloud layers (Proske et al., 2021).
66         Primary ice formation in MPCs is catalyzed by the action of ice nucleating particles
67    (INPs) (e.g., Hoose and Möhler, 2012, Kanji et al., 2017). However, in-situ observations of
68    MPCs in orographic environments regularly reveal that measured ice crystal number
69    concentrations (ICNCs) are several orders of magnitude more abundant than INPs (Rogers and
70    Vali, 1987; Geerts et al., 2015; Lloyd et al., 2015; Beck et al., 2018; Lowenthal et al., 2019;
71    Mignani et al., 2019). Model simulations of alpine MPCs frequently fail to reproduce the

72  elevated ICNCs dictated by observations (Farrington et al., 2016; Henneberg et al., 2017;
73  Dedekind et al., 2021).

74      The inability of primary ice to reproduce the observed ICNCs in orographic MPCs has
75  often been attributed to the influence of surface processes including lofting of snowflakes (i.e.,
76  "blowing snow"; Rogers and Vali, 1987; Geerts et al., 2015), detachment of surface hoar frost
77  (Lloyd et al., 2015), turbulence near the mountain surface or convergence of ice particles due
78  to orographic lifting (Beck et al., 2018) and riming on snow-covered surfaces (Rogers and Vali,
79  1987). The impact of blowing snow ice particles (BIPS) has been studied thoroughly, either
80  using observations collected in mountainous regions (e.g., Lloyd et al., 2015; Beck et al., 2018;
81  Lowenthal et al., 2019), remote sensing (e.g., Rogers and Vali, 1987; Vali et al., 2012; Geerts
82  et al., 2015) or detailed snow-cover models (e.g., Lehning et al., 2006; Krinner et al., 2018)
83  coupled with atmospheric models (e.g., Vionnet et al., 2014; Sharma et al., 2021. The extent to
84  which BIPS can affect ICNCs in MPCs remains poorly understood.

85      In-cloud secondary ice production (SIP) – or ice multiplication – processes may also
86  enhance ice production above the concentration of INPs (Field et al., 2017; Korolev and
87  Leisner, 2020). Three mechanisms are thought to be responsible for most of the SIP. The first,
88  known as the Hallett-Mossop (HM) process (Hallett and Mossop, 1974), refers to the ejection
89  of small secondary ice splinters after a supercooled droplet with a diameter larger than ~25 μm
90  rimes onto a large ice particle at temperatures between –8 and –3 ˚C (Choularton et al., 1980;
91  Heymsfield and Mossop, 1984). This SIP mechanism is widely implemented in atmospheric
92  models (e.g., Beheng, 1987; Phillips et al., 2001; Morrison et al., 2005), but cannot on its own
93  explain the enhanced ICNCs in remote environments (Young et al., 2019; Sotiropoulou et al.,
94  2020, 2021a), especially for when the conditions required for HM initiation are not fulfilled
95  (e.g., Korolev et al., 2020).

96      Collisional fracturing and breakup (BR) of delicate ice particles with other ice particles
97  (Vardiman, 1978; Griggs and Choularton, 1986; Takahashi et al., 1995) is another important
98  SIP mechanism. Several field studies in the Arctic (Rangno and Hobbs, 2001; Schwarzenboeck
99  et al., 2009), the Alps (Mignani et al., 2019; Ramelli et al., 2021) and laboratory investigations
100 (Vardiman 1978; Takahashi et al. 1995) all show the importance of BR. The latter two studies
101 created the basis for a mechanistic description of BR (e.g., Phillips et al., 2017a; Sullivan et
102 al., 2018a; Sotiropoulou et al., 2020). Parameterizations of BR have recently been implemented
103 in small-scale (Fridlind et al., 2007; Phillips et al., 2017a, b; Sotiropoulou et al., 2020, 2021b;
104 Sullivan et al., 2018a; Yano and Phillips, 2011; Yano et al., 2016), mesoscale (Hoarau et al.,
105 2018; Sullivan et al., 2018b; Qu et al., 2020; Sotiropoulou et al., 2021a; Dedekind et al., 2021)

106 and global climate models (Zhao and Liu, 2021a), each with their own approach towards BR
107 description.

108      Droplet freezing and shattering (DS) is a third SIP mechanism that can produce
109 significant amounts of ice crystals. It occurs when drizzle-size drops (diameter exceeding 50
110 μm) comes in contact with an ice particle or INP. A solid ice shell is initially formed around
111 the droplet (e.g., Griggs and Choularton, 1983), and as it thickens begins building up pressure
112 that leads to breakup in two halves, cracking, bubble burst or jetting (e.g., Keinert et al., 2020).
113 Ejection of small ice fragments may occur, the number of which varies considerably (Lauber
114 et al., 2018; Keinert et al., 2020; Kleinheins et al., 2021; James et al., 2021). Experimentally,
115 fragmentation rate maximizes at temperatures between ~ –10 and –15 $^{\circ}$C (Leisner et al., 2014;
116 Lauber et al., 2018; Keinert et al., 2020). DS can dominate in convective updrafts (Lawson et
117 al., 2015; Phillips et al., 2018; Korolev et al., 2020; Qu et al., 2020). Remote sensing of warm
118 Arctic MPCs suggest DS can be much more conducive to SIP than the HM process (Luke et
119 al., 2021). Single-column simulations by Zhao et al. (2021) support this, but is in contrast with
120 small-scale modeling studies (Fu et al., 2019; Sotiropoulou et al., 2020). Mesoscale model
121 simulations of winter alpine clouds formed at temperatures lower than –8 $^{\circ}$C indicate that DS
122 is not active (Dedekind et al., 2021), while field observations suggest the increasing efficiency
123 of the mechanism at temperatures warmer than –3 $^{\circ}$C (Lauber et al., 2021).

124      Orographic ICNCs in MPCs exceeded the predicted INPs by 3 orders of magnitude,
125 reaching up to ~1000 $L^{-1}$ at –15 $^{\circ}$C during the Cloud and Aerosol Characterization Experiment
126 (CLACE) 2014 campaign at the Jungfraujoch (JFJ) station in the Swiss Alps (Lloyd et al.
127 2015). Although the efficiency of BR and DS peaks at around the same temperature, Lloyd et
128 al. (2015) did not find evidence for their occurrence. Instead, at periods when there was a strong
129 correlation between horizontal wind speed and observed ICNC they suggested that BIPS is
130 contributing to the latter, but could not get ICNCs to exceed ~100 $L^{-1}$. In the absence of such
131 correlation, a flux of hoar frost crystals was considered responsible for the very high ice
132 concentration events (ICNCs > 100 $L^{-1}$), albeit without any direct evidence. Farrington et al.
133 (2016) showed that the inclusion of the HM process upwind of JFJ could not explain the
134 measured concentrations of ice, while the addition of a surface flux of hoar crystals provided
135 the best agreement with observations.

136      Although surface-originated processes have been frequently invoked to explain the
137 disparity between ICNCs and INPs, the role of SIP processes – especially the BR and the DS
138 mechanism – has received far less attention and is addressed in this study. We utilize the
139 Weather Research and Forecasting model (WRF) to conduct simulations of two case studies

140   observed in winter during the CLACE 2014 campaign. Our primary objective is to investigate

141   if the implementation of two SIP parameterizations that account for the effect of BR and DS

142   can reduce the discrepancies between observed and simulated ICNCs. Additionally, we aim to

143   identify the conditions favoring the initiation of SIP in the orographic terrain and explore the

144   synergistic influence of SIP with wind-blown ice.

145

## 2.   Methods

147   2.1 CLACE instrumentation

148   CLACE is a long-established series of campaigns taking place for over two decades at the

149   mountain-top station of JFJ, located in the Bernese Alps, in Switzerland, at an altitude of ~3580

150   m above sea level (a.s.l.) (e.g., Choularton et al., 2008). The measurement area is very complex

151   and heterogeneous with distinct mountain peaks (Fig. 1), while JFJ is covered by clouds

152   approximately 40% of the time, offering an ideal location for microphysical observations

153   (Baltensperger et al., 1998). Owing to the local orography surrounding the site, the wind flow

154   is constrained to two directions (Ketterer et al., 2014). Under southeasterly (SE) wind

155   conditions, air masses are lifted along the moderate slope of the Aletsch Glacier, whereas under

156   northwesterly (NW) wind conditions the air is forced to rise faster along the steep north face

157   of the Alps, which is associated with persistent MPCs (Lohmann et al., 2016). A detailed

158   description of the in-situ and remote sensing measurements taken during January and February

159   2014 as part of the CLACE 2014 campaign is provided by Lloyd et al. (2015) and Grazioli et

160   al. (2015). Here we only offer a brief presentation of the datasets used in this study.

161   Shadowgraphs of cloud particles were produced by the two-dimensional stereo

162   hydrometeor spectrometer (2D-S; Lawson et al., 2006), part of a three-view cloud particle

163   imager (3V-CPI) instrument. The 2D-S products have been used to provide information on the

164   number concentration and size distribution of particles in the size range of 10-1280 μm.

165   Following Crosier et al. (2011), the raw data were processed to distinguish ice crystals from

166   droplets. Removal of artefacts from shattering events was also considered (Korolev et al.,

167   2011), however analysis of the probe imagery (Crosier et al., 2011) along with inter-arrival

168   time histograms did not reveal the presence of shattered particles, presumably because of the

169   much lower velocity at which the 2D-S probe was aspirated (~15 ms$^{-1}$) compared to those

170   during aircraft deployments (Lloyd et al., 2015). An approximation of the ice water content

171   (IWC) at JFJ could also be derived by the 2D-S data using the Brown and Francis (1995) mass-

172   diameter relationship with an uncertainty of up to 5 times (Heymsfield et al., 2010).

173     Additionally, the quantification of the liquid water content (LWC) is based on the liquid droplet

174     size distribution data derived from a DMT cloud droplet probe (CDP; Lance et al., 2010) over

175     the size range between 2 and 50 μm. Meteorological parameters (e.g., temperature, relative

176     humidity, wind speed and wind direction), were provided by MeteoSwiss and used to evaluate

177     the model.

178

179     2.2 WRF simulations

180     WRF version 4.0.1, with augmented cloud microphysics to include the effects of all SIP

181     mechanisms (Sotiropoulou et al., 2021a) is used for non-hydrostatic cloud-resolving

182     simulations. The model has been run with three two-way nested domains (Fig. 1), with a

183     respective horizontal resolution of 12, 3 and 1 km. Two-way grid nesting is generally found to

184     improve the model performance in the inner domain (e.g., Harris and Durran, 2010), although

185     the sensitivity of the results to the applied nesting technique has been shown to be negligible

186     (not shown). The parent domain consists of 148×148 grid points centered over the JFJ station

187     (46.55°N, 7.98°E, shown with a black dot in Fig. 1), while the second and the third domain

188     include 241×241 and 304×304 grids, respectively. The Lambert conformal projection is

189     applied to all three domains, as it is well-suited for mid-latitudes. Here we adapted the so-called

190     "refined" vertical grid spacing proposed by Vignon et al. (2021), using 100 vertical eta levels

191     up to a model top of 50 hPa (i.e., ~20 km). This set-up provides a refined vertical resolution of

192     ~100 m up to mid-troposphere at the expense of the coarsely resolved stratosphere. To

193     investigate the dynamical influence on the development of MPCs under the two distinct wind

194     regimes prevailing at JFJ (Section 2.1), we simulate two case studies, starting on 25 January

195     and 29 January 2014, 00:00 UTC, respectively. Both case studies are associated with the

196     passage of frontal systems over the region of interest, approaching the alpine slopes either from

197     the NW (cold front) or the SE (warm front) direction, as shown by the vertically-integrated

198     condensed water content (ICWC; sum of cloud droplets, rain, cloud ice, snow, and graupel) in

199     Fig. 1. For both cases the simulation covers a 3-day period, with the first 24 hours being

200     considered sufficient time for spin up. A 27-s time step was used in the parent domain and goes

201     down to 9 s in the second domain and 3 s in the third domain. Note that achieving such small

202     time steps in the innermost domain is essential to ensure numerical stability in non-hydrostatic

203     simulations over a region with complex orography such as around JFJ.

204
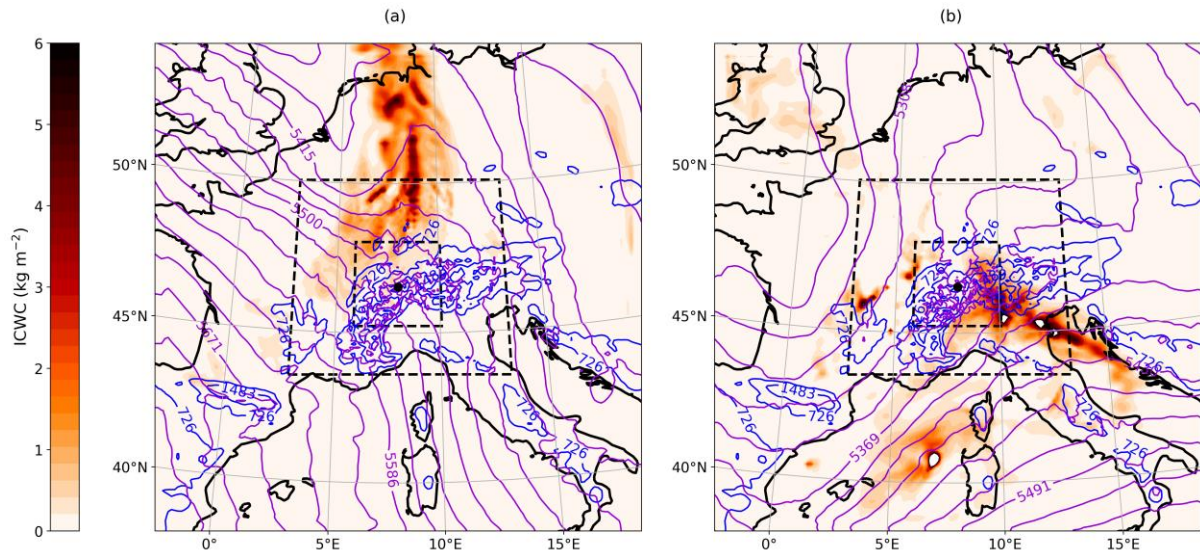
205
206 **Figure 1.** Map of synoptic conditions around JFJ station at (a) 00:00 UTC, 26 January 2014
207 and (b) 00:00 UTC, 30 January 2014, from the control simulation (12-km resolution domain).
208 The purple (blue) contours show the 500 hPa geopotential height in m (the terrain heights in
209 m). The color shading shows the vertically-integrated condensed water content (in kg m$^{-2}$). The
210 black dashed lines delimit the 3-km and 1-km resolution domains, while the black dot locates
211 the JFJ station.

212

213     The fifth generation of the European Centre for Medium-Range Weather Forecasts
214 (ECMWF) atmospheric reanalyses dataset (ERA5; Hersbach et al., 2020) is used to initialize
215 the model and provide the lateral forcing at the edge of the 12-km resolution domain every 6
216 hours. Static fields at each model grid point come from default WRF pre-processing system
217 datasets, with a resolution of 30″ for both the topography and the land use fields. Land use
218 categories are based on the Moderate Resolution Imaging Spectroradiometer (MODIS) land-
219 cover classification. Regarding the physics options chosen to run WRF simulations, the Rapid
220 Radiative Transfer Model for general circulation models (RRTMG) radiation scheme is applied
221 to parameterize both the short-wave and long-wave radiative transfer. The vertical turbulent
222 mixing is treated with the Mellor-Yamada-Janjic (MYJ; Janjić, 2002) 1.5 order scheme, while
223 surface options are modeled by the Noah land-surface model (Noah LSM; Chen and Dudhia,
224 2001). The Kain-Fritsch cumulus parameterization has been activated only in the outermost
225 domain, as the resolution of the two nested domains is sufficient to reasonably resolve cumulus-
226 type clouds at grid-scale.

227

228  *2.2.1 Microphysics scheme and primary ice production*

229  The Morrison two-moment scheme (Morrison et al., 2005; hereafter M05) is used to

230  parameterize the cloud microphysics, following the alpine cloud study of Farrington et al.

231  (2016). The scheme includes double-moment representations of rain, cloud ice, snow and

232  graupel species, while cloud droplets are treated with a single-moment approach and therefore

233  the cloud droplet number concentration ($N_d$) must be prescribed. Here $N_d$ is set to 100 cm$^{-3}$,

234  based on the mean $N_d$ observed within the simulated temperature range (Lloyd et al., 2015).

235  Three primary ice production mechanisms through heterogeneous nucleation are

236  described in the default version of the M05 scheme, namely immersion freezing, contact

237  freezing, and deposition/condensation freezing nucleation. Immersion freezing of cloud

238  droplets and raindrops is described by the probabilistic approach of Bigg (1953). Contact

239  freezing is parameterized following Meyers et al. (1992). Finally, deposition and condensation

240  freezing is represented by the temperature-dependent equation derived by Rasmussen et al.

241  (2002) based on the in-situ measurements of Cooper (1986) collected from different locations

242  at different temperatures. Following Thompson et al. (2004), this parameterization is activated

243  either when there is saturation with respect to liquid water and the simulated temperatures are

244  below –8 °C or when the saturation ratio with respect to ice exceeds a value of 1.08. The

245  accuracy of these parameterizations in representing atmospheric INPs is debatable as they are

246  derived from very localized measurements over a limited temperature range. Nevertheless,

247  Farrington et al. (2016) argued that the deposition/ condensation freezing parameterization of

248  Cooper (1986) can effectively explain INPs between the range 0.01 and 10 L$^{-1}$, which is

249  frequently observed during field campaigns at JFJ (Chou et al., 2011; Conen et al., 2015).

250

251  *2.2.2 Ice multiplication through rime splintering in the M05 scheme*

252  Apart from primary ice production, the HM process is the only SIP mechanism included in the

253  default version of the M05 scheme. This parameterization adapted from Reisner et al. (1998),

254  based on the laboratory findings of Hallett and Mossop (1974), allows for splinter production

255  after cloud- or rain- drops are collected by rimed snow particles or graupel. The efficiency of

256  this process is zero outside the temperature range between –8 and –3 °C, while it follows a

257  linear temperature-dependent relationship in between. HM is not activated unless the rimed ice

258  particles have masses larger than 0.1 g kg$^{-1}$ and cloud or rain mass mixing ratio exceeds the

259  value of 0.5 g kg$^{-1}$ or 0.1 g kg$^{-1}$, respectively. Since these conditions are rarely met in natural

260  MPCs, previous modeling studies had to artificially remove any thresholds to achieve an

261  enhanced efficiency of this process (Young et al., 2019; Atlas et al., 2020). In the current study,
262  however, the HM process is not effective, as the simulated temperatures at JFJ altitude are
263  below –8 °C (see Sect. 2.3).
264

265  *2.2.3 Ice multiplication through ice-ice collisions in the M05 scheme*
266  In addition to the HM process, we have also included two parameterizations to represent the
267  BR mechanism. An extensive description of the implementation method is provided in
268  Sotiropoulou et al. (2021a) (see their Appendix B). Among the three ice particle types included
269  in the M05 scheme (i.e., cloud ice, snow, graupel), we assume that only the collisions between
270  cloud ice-snow, cloud ice-graupel, graupel-snow, snow-snow, and graupel-graupel can result
271  in ice multiplication. The first parameterization tested here follows the simplified methodology
272  proposed by Sullivan et al. (2018a), which is based on the laboratory work of Takahashi et al.
273  (1995). Their findings revealed a strong temperature dependence of the fragment numbers
274  generated per collision ($N_{BR}$):

$$N_{BR} = 280 \, (T - T_{min})^{1.2} e^{-(T-T_{min})/5} \, , \tag{1}$$

275  where $T_{min} = 252 \, K$, is the minimum temperature for which BR occurs. Yet their experimental
276  set-up was rather simplified involving only collisions between large hail-sized ice spheres with
277  diameters of ~2 cm. Taking this into account, Sotiropoulou et al. (2021a) further scaled the
278  temperature-dependent formulation for size:

$$N_{BR} = 280 \, (T - T_{min})^{1.2} e^{-(T-T_{min})/5} \, \frac{D}{D_0} \, , \tag{2}$$

279  where *D* is the size in meters of the particle that undergoes break-up and $D_0$=0.02 m is the size
280  of the hail-sized balls used in the experiments of Takahashi et al. (1995).
281      Phillips et al. (2017a) proposed a more physically-based formulation, developing an
282  energy-based interpretation of the experimental results conducted by Vardiman (1978) and
283  Takahashi et al. (1995). The initial collisional kinetic energy is considered as the governing
284  constraint driving the BR process. Moreover, the predicted $N_{BR}$ depends on the ice particle type
285  and morphological habit and is a function of the temperature, particle size and rimed fraction.
286  Here the generated fragments per collision are described as follows:

$$N_{BR} = aA \left( 1 - exp \left\{ - \left[ \frac{CK_0}{aA} \right]^\gamma \right\} \right) , \tag{3}$$

287  where $K_0 = \frac{1}{2} \frac{m_1 m_2}{m_1+m_2} (\Delta u_{n12})^2$ is the initial kinetic energy, in which $m_1$ and $m_2$ are the masses
288  of the colliding particles and $|\Delta u_{n12}| = \{(1.7 \, u_{n1} - u_{n2})^2 + 0.3 \, u_{n1} \, u_{n2}\}^{1/2}$ is the difference

289   in their terminal velocities. The correction term is proposed by Mizuno et al. (1990) and Reisner

290   et al. (1998) to account for underestimates when $u_{n1} \approx u_{n2}$. The parameter $a$ in Eq. 3 is the

291   surface area of the smaller ice particle (or the one with the lower density), defined as $a = \pi D^2$,

292   with $D$ as in Eq. 2. $A$ in Eq. 3 represents the number density of breakable asperities on the

293   colliding surfaces. For collisions that involve cloud ice and snow particles $A$ is described as

294   $A = 1.58 \times 10^7 (1 + 100\Psi^2)(1 + \frac{1.33 \times 10^{-4}}{D^{1.5}})$, where $\Psi < 0.5$ is the rimed fraction of the most

295   fragile ice particle. For graupel-graupel collisions $A$ is given by a temperature-dependent

296   equation as $A = \frac{a_0}{3} + \max(\frac{2a_0}{3} - \frac{a_0}{9}|T - 258|, 0)$, in which $a_0 = 3.78 \times 10^4 \left(1 + \frac{0.0079}{D^{1.5}}\right)$. $C$

297   is the asperity-fragility coefficient, which is empirically derived to account for different

298   collision types, while the exponent $\gamma$ is equal to 0.3 for collisions between graupel-graupel and

299   is calculated as a function of the rimed fraction for collisions including cloud ice and snow.

300   The parameterization was developed based on particles with diameters 500 μm $< D <$ 5 mm,

301   however Phillips et al. (2017a) suggest that it can be used for particle sizes outside the

302   recommended range as long as the input variables to the scheme are set to the nearest limit of

303   the range. Finally, since $N_{BR}$ was never observed to exceed 100 in the experiments of Vardiman

304   (1978), here we also use this value as an upper limit for all collision types (Phillips et al.,

305   2017a). All predicted fragments emitted through BR are added to the cloud ice category.

306

307   *2.2.4 Ice multiplication through droplet shattering in the M05 scheme*

308   Two different parameterizations are implemented in the M05 scheme to investigate the

309   potential efficiency of the DS mechanism in producing secondary ice splinters ($N_{DS}$). Phillips

310   et al. (2018) proposed two possible modes of raindrop-ice collisions, that can initiate the

311   freezing process. In the first mode, the freezing of the drop occurs either by collecting a small

312   ice particle or through heterogeneous freezing. In the default M05 scheme, the product of

313   collisions between raindrops and cloud ice is considered to be graupel (snow) – if the rain

314   mixing ratio is greater (lower) than 0.1 g kg$^{-1}$, following Reisner et al. (1998). Additionally,

315   the heterogeneous freezing of big raindrops in immersion mode follows Bigg's (1953)

316   parameterization (Section 2.2.1). Here we consider that the product of these two processes can

317   undergo shattering and generate numerous ice fragments, the number of which is parameterized

318   after Phillips et al. (2018). The formulation is derived by fitting multiple laboratory datasets to

319   a Lorentzian function of temperature and a polynomial expression of the drop size. More

320   precisely, the total number of fragments ($N$) generated per frozen drop are given by:

$$N = \varXi(D_r)\varOmega(T)\left[\frac{\zeta\eta^2}{(T-T_0)^2+\eta^2} + \beta T\right], \tag{4}$$

where T is the temperature (in K) and $D_r$ is the size of the freezing raindrop (in mm). Note that $N$ is defined as the sum of the big fragments ($N_B$) and tiny splinters ($N_T$). Equation (4) applies only to drop diameters less than 1.6 mm, which is the maximum observed experimentally. For droplet sizes beyond this maximum value, $N$ can be inferred by linear extrapolation. $N_B$ is described by another Lorentzian:

$$N_B = min\left\{\varXi(D_r)\varOmega(T)\left[\frac{\zeta_B\eta_B^2}{\left(T-T_{B,0}\right)^2+\eta_B^2}\right], N\right\}. \tag{5}$$

The factors $\varXi(D_r)$ and $\varOmega(T)$ in Eq. (4) and (5) are cubic interpolation functions, impeding DS for $D_r < 0.05$ mm and T > −3 °C. Furthermore, the parameters $\zeta$, $\eta$, $T_0$, $\beta$, $\zeta_B$, $\eta_B$, $T_{B,0}$, are analytically described in Phillips et al. (2018). That the big fragments emitted (i.e., $N_B$) will be initiated in the model as graupel, snow or frozen drops, while only the splinters ($N_T = N - N_B$) are considered secondary ice (i.e., $N_{DS} = N_T$) and are passed to the cloud ice category.

The second mode of raindrop-ice collisions includes the accretion of raindrops on impact with more massive ice particles, such as snow or graupel, the description of which in the M05 scheme is adapted from Ikawa and Saito (1991). While there is only one dedicated laboratory study of this SIP mode (James et al., 2021), it was also indirectly investigated in the experimental study of Latham and Warwicker (1980), who reported that the collision of supercooled raindrops with hailstones can generate secondary ice. Phillips et al. (2018) proposed an empirical, energy-based formulation to account for the tiny splinters ejected after collisions between raindrops and large ice particles:

$$N_{DS} = 3\varPhi(T) \times [1 - f(T)] \times max(DE - DE_{crit}, 0) \ , \tag{6}$$

where $DE = \frac{K_0}{S_e}$, is the dimensionless energy given as the ratio of the initial kinetic energy ($K_0$; described in 2.2.3) over the surface energy, which is expressed by the product $S_e = \gamma_{liq}\pi D_r^2$, in which $\gamma_{liq}$=0.073 J m$^{-2}$, is the surface tension of liquid water. The critical value of DE used in Eq. (6) for the onset of splashing upon impact is set to $DE_{crit} = 0.2$. The parameter $f(T) = -c_w T/L_f$, represents the initial frozen fraction of a supercooled drop during the first stage of the freezing process, where $C_w = 4200$ J kg$^{-1}$ K$^{-1}$, is the specific heat capacity of liquid water, $L_f = 3.3 \times 10^5$ J kg$^{-1}$, is the specific latent heat of freezing, while T is the initial freezing temperature (°C) of the raindrop. Finally, $\varPhi(T) = min[4f(T),1]$ is an empirical fraction, which represents the probability of any new drop in the splash products to contain a frost secondary

348 ice particle. At temperatures ~ –10 $^{\circ}$C this formulation yields $\Phi = 0.5$, meaning that the

349 probability of a secondary drop to contain ice is 50%. James et al. (2021) provided the first

350 laboratory study to constrain this parameter. Further details regarding the derivation of the

351 empirical parameters and the uncertainties underlying the mathematical formulations are

352 discussed in Phillips et al. (2018).

353      The second DS parameterization tested in this study was developed by Sullivan et al.

354 (2018a) and is a function of the freezing droplet diameter ($D_r$ in μm), a shattering probability

355 ($p_{sh}$) and a freezing probability ($p_{fr}$):

$$N_{DS} = 2.5 \times 10^{-11} D_r{}^4 \, p_{sh} \, p_{fr} \; . \tag{7}$$

356 The diameter dependence describing the fragment numbers generated per fractured frozen

357 droplet is derived by nudging the liquid water and ice particle size distributions in one-

358 dimensional cloud model simulations towards aircraft observations collected in tropical

359 cumulus clouds (Lawson et al., 2015). The $p_{sh}$ is based upon droplet levitation experiments

360 shown in Leisner et al. (2014) and is represented by a temperature-dependent Gaussian

361 distribution, centered at ~ –15 $^{\circ}$C. Note that $p_{sh}$ is non-zero only for droplets with sizes greater

362 than 50 μm. The $p_{fr}$ is 0 for temperatures warmer than –3 $^{\circ}$C and 1 if temperatures fall below –

363 6 $^{\circ}$C, following the cubic interpolation function, $\Omega(T)$, adapted from Phillips et al. (2018).

364

365 2.3 Model validation

366 The control simulation (CNTRL), performed with the standard M05 scheme, sets the basis for

367 assessing the validity of the model against available meteorological observations. Temperature,

368 relative humidity, wind speed, and wind direction are obtained from the MeteoSwiss weather

369 station at JFJ. The comparison of each meteorological variable with the results from the nearest

370 model grid point of the CNTRL simulation is shown in Fig. 2. Note that the outputs are from

371 the first atmospheric level of the innermost domain at ~10 m above ground level (a.g.l) (Fig.

372 1), while the first 24 hours of each simulation period are considered spin up time and are

373 therefore excluded from the present analysis. The mean modeled values and standard

374 deviations (std), along with the root mean square error (RMSE) and the index of agreement

375 (IoA) between model predictions and observational data are summarized in Table 1. IoA is

376 both a relative and a bounded measure (i.e., $0 \leq \text{IoA} \leq 1$) that describes phase errors between

377 predicted ($P_i$) and observed ($O_i$) time series (Willmott et al., 2012):

$$IoA = 1 - \left[ \frac{\sum_{i=1}^{N}(P_i - O_i)^2}{\sum_{i=1}^{N}(|P_i'| - |O_i'|)^2} \right] \, , \tag{8}$$

378    where $P_i' = P_i - \bar{O}$ and $O_i' = O_i - \bar{O}$, in which $\bar{O}$ is the mean of the observed variable.

379
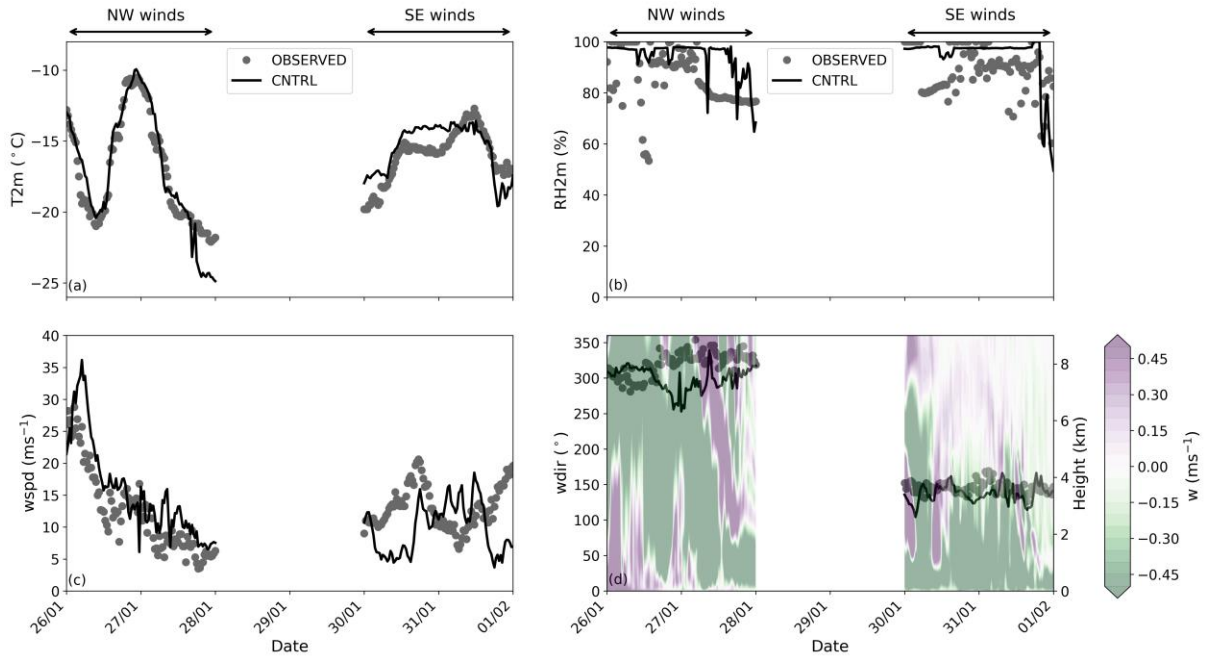
380
381    **Figure 2.** Time series of (a) temperature (T2m), (b) relative humidity with respect to liquid
382    phase at 2m height (RH2m), (c) wind speed (wspd) and (d) wind direction (wdir). Grey circles
383    indicate measurements collected between 26 January and 1 February 2014 at JFJ station, while
384    modeled values from CNTRL simulation are shown with a black line. The semi-transparent
385    contour plot is representing the vertical velocity (w) profile predicted by the CNTRL
386    simulation. Each day starts at 00:00 UTC.

387

388          Throughout the two case studies, the WRF simulations seem to closely follow the
389    observed temperatures (Fig. 2a), which is also indicated by the high IoA in Table 1. The
390    synoptic situation occurring on 26 January, with a deep trough extending to western Europe
391    (Fig. 1), has been associated with intense snowfalls in the alpine regions (Panziera and Hoskins,
392    2008). The passage of the cold front was followed by a sharp temperature decrease, with the
393    simulated temperatures fluctuating between –10 and ~ –20 °C throughout the NW case (Fig.
394    2a). Under the influence of the warm front during the SE case, the modeled temperatures rose
395    from ~ –18 °C to ~ –14 °C and remained less variable until 30 January 12:00 UTC, with mean
396    values of ~ –15.5 °C (Table 1).

397

**Table 1.** Mean modeled values (± standard deviations), RMSE and IoA between the CNTRL simulation of WRF and measurements carried out by the MeteoSwiss station at JFJ.

| Variable | Mean ± std | | RMSE | | IoA | |
|---|---|---|---|---|---|---|
| | NW winds | SE winds | NW winds | SE winds | NW winds | SE winds |
| T2m (˚C) | -17.10 ± 4.36 | -15.48 ± 1.75 | 1.40 | 1.33 | 0.97 | 0.84 |
| RH2m (%) | 94.07 ± 7.02 | 94.24 ± 10.31 | 14.01 | 11.61 | 0.55 | 0.64 |
| wspd (ms$^{-1}$) | 15.57 ± 7.45 | 9.78 ± 3.94 | 4.85 | 6.75 | 0.88 | 0.22 |

Fig. 2c and 2d reveal that the 1-km resolution domain can sufficiently capture the local wind systems to a certain extent. During the NW flow, the horizontal wind speeds are reproduced better by the CNTRL simulation (IoA=88%), whereas during the SE winds, the simulated wind speed is frequently underestimated compared with observations (Fig. 2c). Such deviations in the horizontal wind speed might be caused by the relatively coarse horizontal resolution of the model, which prevents some small-scale and very local orographic structures from being resolved. As discussed in Section 2.2, the observed winds at JFJ are channeled by the orography to either NW or SE directions. The CNTRL simulation of WRF can satisfactorily reproduce the wind direction in both cases, although the simulated values exhibit larger fluctuations than the measured ones (Fig. 2d), presumably because of the surrounding orography being less accurately represented in the model. This is particularly evident during NW winds, when the simulated wind directions shift slightly to west directions compared to observations. The positive vertical velocities, illustrated in the contour plot in Fig. 2d, result from the orographically forced lifting of the airmasses over the local topography, and are not related to convective instability in the lower atmospheric levels. The stronger updrafts prevailing until the end of 26 January are associated with the steep ascent of the air parcels, which can also contribute to the enhanced relative humidity (Fig. 2b). After the frontal passage, the vertical velocities at the lower levels are downward directed, with the vertical profile of potential temperature revealing that the atmosphere at JFJ is stabilized (not shown). The same vertical velocity pattern, with mainly downward motions, characterizes the stably stratified atmosphere after 30 January. Overall, Fig. 2 suggests that local meteorological conditions at JFJ are reasonably well represented by the model.

424 2.4 Model simulations

425 Given the good representation of the atmospheric conditions at JFJ, the CNTRL simulation of

426 WRF is further accompanied by five sensitivity simulations, aiming to investigate the

427 contribution of BR and DS mechanisms. Here we also perform three additional sensitivity

428 experiments to explore the potential impact of blowing ice and the synergistic interaction with

429 SIP on the development of the simulated MPCs. A detailed list of the sensitivity experiments

430 is provided in Table 2.

431   The contribution of the DS mechanism is addressed in two sensitivity experiments,

432 DS_PHILL and DS_SULL, where the parameterizations of Phillips et al. (2018) and Sullivan

433 et al. (2018a) were applied, respectively (Section 2.2.4). Both sensitivity simulations yield

434 predictions that coincide with the CNTRL simulation (supplement Fig. S1) suggesting that the

435 DS mechanism is hardly ever activated, and fail to produce realistic total ice number

436 concentrations ($N_{isg}$; cloud ice + snow + graupel). The absence of correlation between LWC

437 and $N_{isg}$ fluctuations might also suggest the ineffectiveness of this mechanism under the

438 examined conditions. Note that the parameterized expressions used to describe the DS

439 mechanism involve a number of empirical and rather uncertain parameters, the value of which

440 could potentially influence the efficiency of the process in producing secondary ice fragments.

441 However, the sensitivity of our results to the choice of these parameters would be negligible,

442 as the low concentrations ($\lesssim 10^{-2}$ cm$^{-3}$) of relatively small raindrops with mode diameters

443 below the threshold size of 50 μm seem to completely prevent the onset of the DS process

444 (supplement Fig. S2). The DS mechanism is therefore excluded from the following discussion.

445 This result is in line with the modeling study of Dedekind et al. (2021), who also reported the

446 inefficiency of this mechanism in wintertime alpine clouds.

447   Three sensitivity simulations are also conducted activating the generation of secondarily

448 formed ice particles through BR. First, the TAKAH simulation, adopts the temperature-

449 dependent formula of Takahashi et al. (1995) scaled with the size of particles that undergo

450 fragmentation (Sotiropoulou et al. 2021a). Applying Equation (2) to collisions between all ice

451 categories considered in the M05 scheme (except collisions between cloud-ice particles;

452 Section 2.2.3) inserts a caveat to our approach. The laboratory results of Takahashi et al. (1995)

453 suggest that, it is mostly the collisions between rimed particles and graupel that are more

454 conducive to SIP through BR. Vardiman (1978) also reported that ice crystal growth through

455 riming is essential to boost fragmentation. Applying the Takahashi break-up scheme for

456 unrimed ice particles might, therefore, overestimate the number of secondary ice fragments.

457 To test this hypothesis, we performed TAKAHrim sensitivity simulation, where we enabled

458 ice multiplication through BR only after collisions between rimed cloud ice/ snow and graupel
459 particles. To diagnose the presence of rime on ice particles we used the amount of cloud
460 droplets or raindrops accreted by snow and cloud ice, which is predicted in the M05 scheme.
461

462 **Table 2.** List of sensitivity simulations conducted with WRF.

| Simulation | BR process | DS process | NBIPS ($L^{-1}$) |
|---|---|---|---|
| CNTRL | off | off | 0 |
| DS_PHILL | off | Phillips et al., 2018 | 0 |
| DS_SULL | off | Sullivan et al., 2018a | 0 |
| TAKAH | Takahashi et al., 1995 | off | 0 |
| TAKAHrim | Takahashi et al., 1995 activated only after collisions between rimed ice particles | off | 0 |
| PHILL | Phillips et al., 2017a | off | 0 |
| BIPS10 | off | off | 10 |
| BIPS100 | off | off | 100 |
| BIPS100_PHILL | Phillips et al., 2017a | off | 100 |

463

464 Finally, the performance of the more advanced Phillips et al. (2017a) parameterization is
465 tested in the PHILL simulation. Parameters involved in the Phillips parameterization that are
466 not explicitly resolved in the M05 microphysics scheme are the rimed fraction and the ice habit
467 of colliding ice particles. The choice of ice habit is based on particle images collected during
468 the CLACE 2014 campaign, showing the presence of non-dendritic sectored plates and oblate
469 particles at temperatures $\sim -15$ $^{\circ}$C (Lloyd et al., 2015). Grazioli et al. (2015) also presented
470 some examples of particle imagery produced by a 2D-S imaging probe, revealing the presence
471 of heavily rimed hydrometeors, as well as highly oblate particles (probably columns or
472 needles). The rimed fraction, is prescribed to a value of 0.4 (0.3) to account, respectively, for
473 heavily and moderately rimed ice particles present under NW (SE) wind conditions. A high
474 degree of riming is expected in the simulated cases, as they both occur under ice-seeding
475 situations (Section 3.1.1), where large precipitating ice particles from the seeder clouds
476 effectively gain mass in the mixed-phase zone through riming. Direct observations with
477 balloon-borne measurements carried out within ice-seeding events in the region around Davos
478 in the Swiss Alps support the presence of a large fraction of rimed particles and graupel

479 (Ramelli et al., 2021). The higher riming degree is prescribed under NW-winds because the
480 orographic forcing (i.e., vertical velocity) is stronger and helps maintaining mixed-phase
481 conditions in the feeder clouds – which in turn promotes ice crystal growth through riming.
482 However, our results were not very sensitive to the choice of the rimed fraction.

483      The remaining sensitivity simulations focus on the potential impact of BIPS. A recently-
484 developed blowing snow scheme, used to simulate alpine snowpacks, reported significant mass
485 and number mixing ratios of BIPS that can be found up to ~1 km above the surface under high
486 wind speed conditions (see Fig. 17 in Sharma et al., 2021) with the potential to trigger cloud
487 microphysical processes. Given that in the default M05 scheme there is no parameterization of
488 a flux of ice particles from the surface, we parameterize the effect of BIPS lofting into the
489 simulated orographic clouds by applying a constant ice crystal source to the first atmospheric
490 level of WRF over the whole model domain. Although the source of BIPS at the first model
491 level remained constant, yet their number will be affected by processes such as advection,
492 sublimation and sedimentation, that are described in the M05 scheme. Note that the relatively
493 coarse horizontal resolution in the innermost domain of our simulations (i.e., 1 km) does not
494 allow the accurate representation of the small-scale turbulent flow over the orographic terrain.
495 This is considered a limitation of our methodology, since turbulent diffusion is a key process
496 affecting the amount of BIPS that will be resuspended from the surface.

497      The applied concentrations of BIPS varied between $10^{-2}$ and 100 $L^{-1}$, which is the upper
498 limit proposed by Lloyd et al. (2015) and observed within in-cloud conditions by Beck et al.
499 (2018). Number concentrations of BIPS (i.e., NBIPS) lower than 10 $L^{-1}$ were found incapable
500 of affecting the simulated cloud properties and are, therefore, not included in the following
501 discussion. Two sensitivity simulations are finally performed, BIPS10 and BIPS100 (Table 2),
502 in which the number indicates the NBIPS in $L^{-1}$. In our approach we assume BIPS are spherical
503 with diameters of 100 μm, based on typical sizes that are frequently reported in the literature
504 (e.g., Schlenczek et al., 2014; Schmidt, 1984; Geerts et al., 2015; Sharma et al., 2021). The
505 relatively small fall speed of these particles (e.g., Pruppacher and Klett, 1997) will allow them
506 to remain suspended in the atmosphere. As a sensitivity we also considered smaller particles
507 with sizes of 10 μm, but our results did not change significantly (supplement Fig. S3).
508 Nevertheless, such small ice particles are not expected to substantially contribute to the
509 simulated IWC, as shown by Farrington et al. (2016).

510      As SIP through BR and blowing snow are both important when trying to explain the high
511 ICNCs observed in alpine environments, their combined effect is addressed in our last
512 simulation, BIPS100_PHILL (Table 2). In this sensitivity simulation the effect of BR is

513    parameterized after Phillips et al. (2017a), while a constant ice crystal concentration of 100 L$^{-1}$

514    is applied to the first atmospheric level of WRF to represent the effect of BIPS.

515

516    **3.    Results and discussion**

517

518    3.1 Impact of SIP through BR on simulated microphysical properties

519    The temporal evolution of $N_{isg}$, IWC and LWC, at the first model level (~ 10 m a.g.l.) from the

520    nearest to JFJ model grid point of the CNTRL, TAKAH and PHILL simulations is presented

521    in Fig. 3. Instead of focusing on a single grid point, we also averaged the results from the 9-

522    km$^2$ area surrounding the point of interest. However, the produced time series showed only

523    little difference when compared to the nearest grid point time series (not shown), ensuring our

524    analysis is robust. Besides, the region in the vicinity of JFJ is very heterogeneous supporting

525    the single point comparison presented in the following discussion. The grey dots shown in Fig.

526    3 represent the measurements taken by the 2D-S and CDP instruments at JFJ throughout the

527    two periods of interest. The displayed time frequency of the observations is 30 min to match

528    the output frequency of the model. Note that the simulated LWC includes liquid water from

529    cloud droplets and rain, while the simulated IWC includes cloud ice, snow and graupel. The

530    contribution of rain in our simulations is, however, negligible (supplement Fig. S2). Several

531    statistical metrics for $N_{isg}$, IWC and LWC are summarized in Table 3, 4 and 5, respectively.

532    Periods with missing data in the measurement time series are excluded from the statistical

533    analysis.

534        During the NW flow, between 26 and 28 January, the measured ICNCs exceed 100 L$^{-1}$

535    for >50 % of the time, whereas during the SE flow the ICNCs usually fluctuate between 10 and

536    100 L$^{-1}$ (Fig. 3a). The highest ICNCs are generally observed at temperatures higher than ~ –15

537    $^{\circ}$C, where SIP processes are thought to be dominant and primary ice nucleation in the absence

538    of bioaerosols is limited (e.g., Hoose and Möhler, 2012; Kanji et al., 2017). The CNTRL

539    simulation fails to reproduce $N_{isg}$ higher than 10 L$^{-1}$, with the mean simulated values being ~2-

540    2.5 L$^{-1}$ during both periods. At the same time the mean observed ICNC values are ~200 (70)

541    L$^{-1}$ during the NW (SE) case. Thus, CNTRL systematically underestimates the amount of ice

542    by up to 2 orders of magnitude, which is also consistent with the interquartile statistics

543    presented in Table 3. With the HM process being totally ineffective in the prevailing

544    temperatures, this discrepancy suggests that ice crystals produced by heterogeneous ice

545 nucleation in CNTRL are not high enough to match the observations. A similar discrepancy

546 between predicted INPs and measured ICNCs was also documented in Lloyd et al. (2015).

547

548 **Table 3.** The $25^{th}$, $50^{th}$ (median) and $75^{th}$ percentiles of ICNC time series (in $L^{-1}$).

| Simulation | 25th perc. | | Median | | 75th perc. | |
|---|---|---|---|---|---|---|
| | NW winds | SE winds | NW winds | SE winds | NW winds | SE winds |
| OBSERVED | 8.69 | 6.64 | 80.47 | 34.53 | 261.25 | 88.69 |
| CNTRL | 0.76 | 0.84 | 2.02 | 1.68 | 2.80 | 3.60 |
| TAKAH | 2.27 | 1.08 | 9.85 | 122.56 | 362.51 | 358.38 |
| TAKAHrim | 2.56 | 0.75 | 12.30 | 4.17 | 101.46 | 82.16 |
| PHILL | 2.49 | 0.76 | 6.27 | 2.09 | 118.21 | 59.23 |
| BIPS10 | 1.60 | 1.90 | 2.42 | 2.72 | 3.30 | 4.78 |
| BIPS100 | 6.17 | 10.74 | 10.36 | 13.88 | 12.32 | 17.39 |
| BIPS100_PHILL | 8.95 | 11.51 | 15.87 | 16.30 | 138.92 | 98.43 |

549

550 Activating the BR process in TAKAH, TAKAHrim and PHILL simulations is found to

551 produce $N_{isg}$ as high as 400 $L^{-1}$ during both case studies (Fig. 3a), resulting in a substantially

552 better agreement with observations. At times when the simulated temperatures drop below ~ –

553 18 $^o$C, the $N_{isg}$ modeled by all three simulations coincide with the CNTRL simulation. At

554 relatively warmer subzero temperatures though, the significant contribution of the BR process

555 is evident, elevating the predicted $N_{isg}$ by up to 3 orders of magnitude during the NW case and

556 by more than 2 orders of magnitude during the SE case. Although the median $N_{isg}$ in all three

557 sensitivity simulations with active break-up remains underestimated compared to observations

558 during the NW flow, TAKAH seems to produce unrealistically high median and $75^{th}$ percentile

559 values during the SE flow (Table 3). Indeed, focusing on the $N_{isg}$ time series (Fig. 3a) TAKAH

560 is ~25% of the time shown to overestimate the observed ICNCs by a factor of ~3, reaching up

561 a factor of 10 on 30 January at 00:00. TAKAHrim and PHILL, on the other hand, produce more

562 reasonable concentrations of ice particles throughout both case studies, with the $N_{isg}$ values in

563 the $75^{th}$ percentile exceeding 100 (50) $L^{-1}$ during the NW (SE) case study (Table 3), which is

564 found to reduce the gap between observations and model predictions.

565 It is worth noting that, despite the fact that the Takahashi parameterization (Eq. 2) is

566 applied to both TAKAH and TAKAHrim simulations, the former seems to systematically

567 overestimate the number of secondary ice fragments, while the latter produces ICNCs that are

568 more consistent with the observations. Hence the Takahashi parameterization predicts

569    reasonable results if it is allowed to generate fragments from collisions between rimed ice

570    particles only (Section 2.4).

571

572    **Table 4.** The $25^{th}$, $50^{th}$ (median) and $75^{th}$ percentiles of IWC (in $gm^{-3}$) time series.

| Simulation | 25th perc. | | Median | | 75th perc. | |
|---|---|---|---|---|---|---|
| | NW winds | SE winds | NW winds | SE winds | NW winds | SE winds |
| OBSERVED | 0.03 | 0.02 | 0.19 | 0.11 | 0.66 | 0.26 |
| CNTRL | $4.3\times10^{-3}$ | $5.0\times10^{-3}$ | 0.03 | 0.04 | 0.15 | 0.12 |
| TAKAH | $1.3\times10^{-3}$ | $2.0\times10^{-3}$ | 0.10 | 0.09 | 0.52 | 0.34 |
| TAKAHrim | $4.7\times10^{-3}$ | $3.1\times10^{-3}$ | 0.08 | 0.04 | 0.33 | 0.27 |
| PHILL | $3.8\times10^{-3}$ | $3.7\times10^{-3}$ | 0.10 | 0.02 | 0.38 | 0.30 |
| BIPS100_PHILL | $3.9\times10^{-3}$ | $9.1\times10^{-3}$ | 0.09 | 0.03 | 0.40 | 0.30 |

573

574         The observed IWC time series (Fig. 3b) are frequently reaching ~1 $gm^{-3}$ during the NW

575    case, with the median values being a factor of 2.5 higher than those observed during the SE

576    case (Table 4). This indicates the presence of more massive ice particles when higher updraft

577    velocities prevail. The CNTRL simulation cannot produce IWC values > 0.8 $gm^{-3}$ and is most

578    of the time below the observed range. Adding a description of the BR process (i.e., in TAKAH,

579    TAKAHrim and PHILL) sufficiently increases the modeled IWC by up to ~1 order of

580    magnitude between 26 January 12:00 UTC and 27 January 06:00 UTC, when the modeled $N_{isg}$

581    exceeds 100 $L^{-1}$ and the temperature remains higher than –16 $^{o}C$. The same conditions are

582    observed in the SE case, between 12:00 and 18:00 UTC on 30 January, when IWC shows a ~3

583    fold enhancement reaching the observed levels. The IWC values in the third quartile predicted

584    by TAKAH, TAKAHrim and PHILL are more than a factor of 2 higher than the ones predicted

585    by CNTRL (Table 4). This increase improves the model performance although the modeled

586    IWC remains slightly underestimated (overestimated) during the NW (SE) case. The size

587    distribution of the three ice species considered in the M05 scheme (supplement Fig. S4) reveals

588    that, the implementation of the BR mechanism leads to elevated concentrations of relatively

589    smaller cloud ice crystals, but at the same time increases the concentrations of snow particles.

590    This is the reason why the modeled total ice mass is also increased compared with the CNTRL

591    simulation.

592         Fig. 3c compares the simulated cloud LWC to the concurrent CDP observations at JFJ.

593    The LWC values recorded during the NW case are highly variant, reaching up to 0.75 $gm^{-3}$,

594    which is substantially higher than the respective maximum LWC observed during the SE case

595 (0.30 gm$^{-3}$). On 26 January before 12:00 UTC, all sensitivity simulations predict LWC > 1 gm$^{-3}$,
596 which, however, cannot be validated against measurements due to missing data in the CDP
597 time series. Note that this period is excluded from the statistics derived in Table 5. The CNTRL
598 simulation is found to overestimate the cloud LWC, predicting 0.42 (0.25) gm$^{-3}$ in the third
599 quartile, which is a factor of ~2 higher than the observed values during the NW (SE) case
600 (Table 5).

601
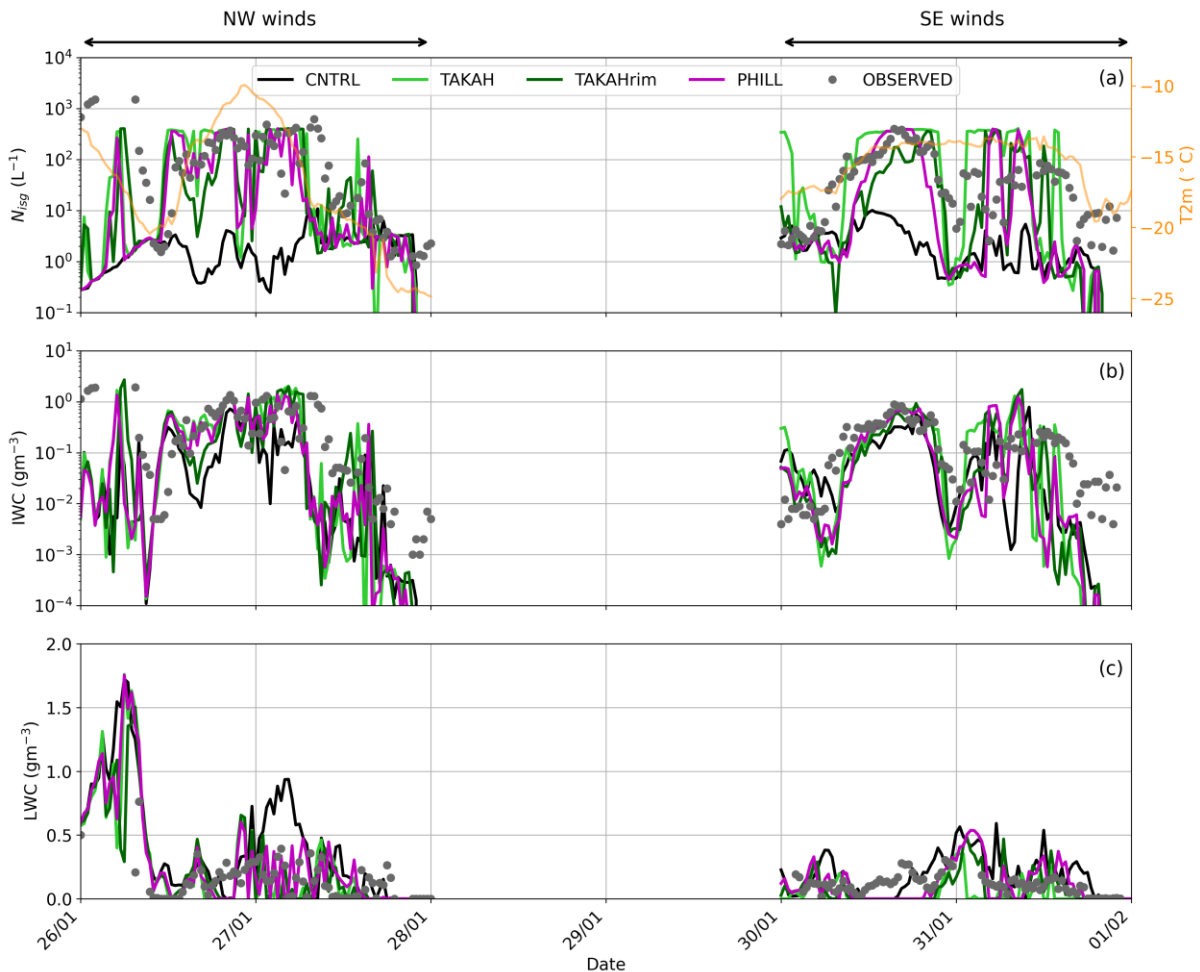
602
603 **Figure 3.** Time series of (a) total $N_{isg}$ and temperature at 2 m height (orange line), (b) IWC and
604 (c) LWC, predicted by the CNTRL (black line), TAKAH (light green line), TAKAHrim (dark
605 green) and PHILL (magenta line) simulations between 26 January and 1 February 2014. The
606 grey dots in all three panels represent the 2D-S ICNCs, the inferred IWC and the CDP LWC
607 measured at the JFJ station, respectively. Note the logarithmic y-axes in panels a and b.

608

609      The modeled LWC in the 75$^{th}$ percentile is decreased by a factor of 1.5-5 in the
610 simulations that account for the BR process (Table 5), improving the agreement with
611 observations (Fig. 3c). The reduction in LWC is expected, considering that the higher $N_{isg}$
612 produced when BR is activated can readily deplete the surrounding droplets under liquid water

613 subsaturated conditions through the WBF process. This introduces a challenging environment
614 to simulate, as the model is sometimes seen to convert water to ice too rapidly, leading to cloud
615 glaciation (e.g., on 30 January after 12:00 UTC). Despite all sinks of cloud water (i.e.,
616 condensation freezing, WBF or riming), observations at JFJ suggest that mixed-phase regions
617 are generally sustained (Lloyd et al., 2015). This is particularly true for the NW case, when the
618 sufficiently large updrafts caused by the steep ascent of the air masses help maintain the
619 supersaturation with respect to liquid water (Lohmann et al., 2016). PHILL and TAKAHrim
620 can more efficiently sustain the observed mixed-phase conditions compared to TAKAH, which
621 frequently results in explosive ice multiplication – especially during the SE case – leading to
622 an underestimation of the LWC (see Fig. 3c and Table 5). TAKAH is, therefore, excluded from
623 the following discussion as it fails to reproduce an accurate liquid and ice partitioning.
624

625 **Table 5.** The $25^{th}$, $50^{th}$ (median) and $75^{th}$ percentiles of LWC (in $gm^{-3}$) time series.

| Simulation | $25^{th}$ perc. | | Median | | $75^{th}$ perc. | |
|---|---|---|---|---|---|---|
| | NW winds | SE winds | NW winds | SE winds | NW winds | SE winds |
| OBSERVED | $8.5\times10^{-3}$ | $70.0\times10^{-3}$ | 0.12 | 0.11 | 0.21 | 0.14 |
| CNTRL | $87.7\times10^{-3}$ | $26.0\times10^{-3}$ | 0.19 | 0.17 | 0.42 | 0.25 |
| TAKAH | $1.3\times10^{-10}$ | 0.0 | 0.01 | $6.7\times10^{-10}$ | 0.16 | 0.05 |
| TAKAHrim | $1.2\times10^{-7}$ | 0.0 | 0.06 | $2.8\times10^{-6}$ | 0.23 | 0.09 |
| PHILL | $6.3\times10^{-8}$ | 0.0 | 0.09 | 0.03 | 0.26 | 0.18 |
| BIPS10 | $82.0\times10^{-3}$ | $4.6\times10^{-3}$ | 0.18 | 0.12 | 0.33 | 0.24 |
| BIPS100 | $67.1\times10^{-3}$ | $13.1\times10^{-3}$ | 0.18 | 0.13 | 0.36 | 0.23 |
| BIPS100_PHILL | $6.3\times10^{-10}$ | 0.0 | 0.09 | 0.06 | 0.27 | 0.10 |

626

627 The time-averaged vertical profiles of cloud ice ($N_i$), graupel ($N_g$), snow ($N_s$) and total
628 $N_{isg}$ number concentrations are illustrated in Fig. 4 for the CNTRL, TAKAHrim and PHILL
629 simulations. The mean $N_i$ (Fig. 4a) and $N_{isg}$ profiles (Fig. 4d) are up to 2 orders of magnitude
630 enhanced in TAKAHrim and PHILL compared to CNTRL. During the NW flow both
631 simulations including the BR process produce similar vertical distribution of the ice
632 hydrometeors in the lowest 1-1.5 km in the atmosphere. This is not the case for the SE case,
633 where TAKAHrim seems to predict a rapid decrease in $N_i$ and $N_s$ and thus in total $N_{isg}$ with
634 altitude. The main difference between these two simulations lies in the fact that the total LWC
635 and hence, the probability of riming, decreases with height limiting the efficiency of BR in
636 TAKAHrim. This become more evident during the SE case where mixed-phase conditions are

637  exclusively confined below 1.5 km in the atmosphere (Section 3.1.1). However, we cannot

638  estimate which vertical distribution better represents reality, due to the lack of corresponding

639  measured profiles. TAKAHrim coincides with PHILL only when there is sufficient liquid water

640  in the atmosphere, allowing for the riming of the ice hydrometeors. Moreover, at heights above

641  ~2.5 km, where the simulated temperatures drop well below –20 °C (supplement Fig. S5), all

642  three simulations are seen to produce similar results. This implies the greater importance of

643  SIP through BR at heights below 2-3 km in the atmosphere (i.e., in the temperature range

644  between ~ –18 °C and ~ –10 °C).

645
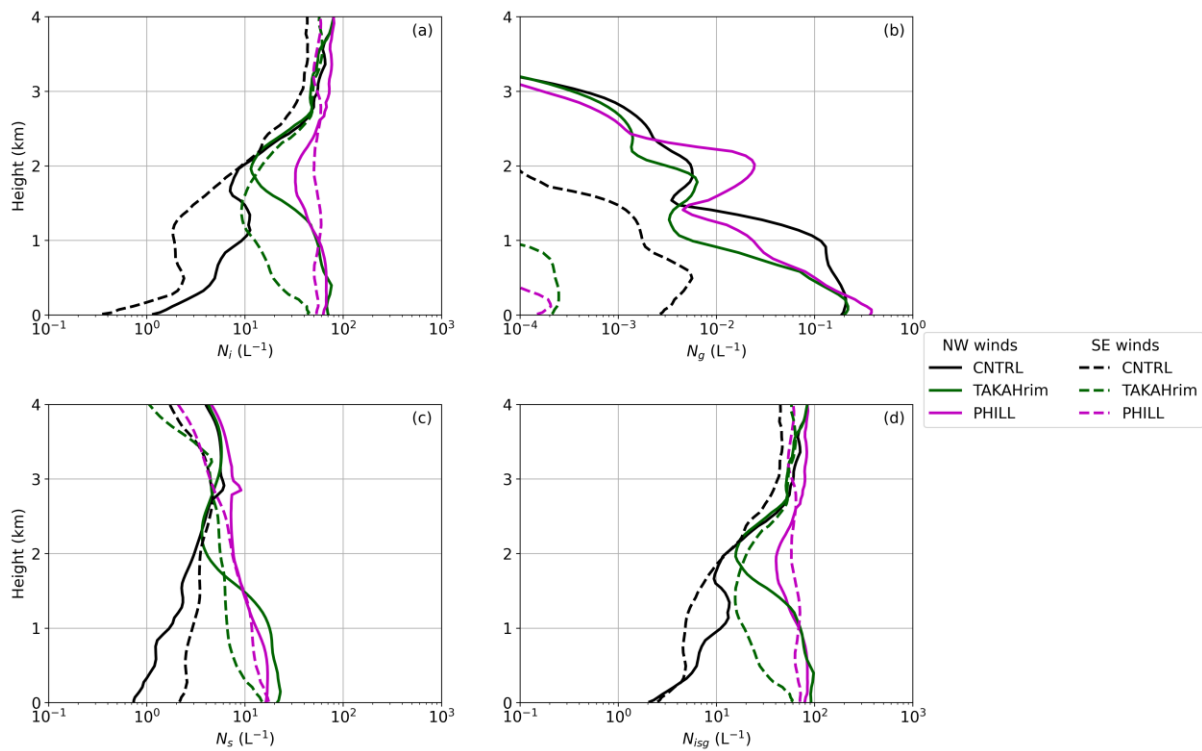
646

647  **Figure 4.** Mean vertical profiles of (a) $N_i$, (b) $N_g$, (c) $N_s$ and (d) total $N_{isg}$, predicted by the
648  CNTRL (black), TAKAHrim (dark green) and PHILL (magenta) simulations for the NW (solid
649  lines) and SE (dashed lines) cases. Note the different scale on the x axis of the $N_g$ vertical
650  distribution. The height is given in km a.g.l.

651

652      Graupel number concentrations (Fig. 4b) do not contribute much to the modeled ice

653  phase, especially during the SE case when the simulated $N_g$ is negligible compared with the $N_i$

654  and $N_s$ (Fig. 4c). In the M05 scheme, portion of the rimed cloud or rain water onto snow is

655  allowed to convert into graupel (Reisner et al. 1998), provided that snow, cloud liquid and rain

656  water mixing ratios exceed a threshold of 0.1, 0.5 and 0.1 g kg$^{-1}$, respectively. These mixing

657  ratio thresholds for graupel formation are arbitrary and might not be suitable for the examined

658    conditions, preventing the formation of graupel from rimed snowflakes (Morrison and

659    Grabowski, 2008). During the NW case, however, we can identify substantially higher $N_g$ than

660    the SE case, owing to the presence of sufficient supercooled liquid water especially during the

661    first half of 26 January. Activating the BR mechanism in TAKAHrim and PHILL generally

662    decreases the simulated $N_g$ in both cases (Fig. 4c), suggesting that break-up of graupel

663    contributes to ice multiplication.

664         The mean vertical profile of $N_s$ (Fig. 4c) seems to follow the respective profile of $N_i$ (Fig.

665    4a). Unlike the graupel concentrations, including the BR mechanism is found to enhance $N_s$ up

666    to one order of magnitude compared to the CNTRL simulation. Focusing on a single model

667    time step when the BR mechanism is activated, the size distribution of snow particles shown

668    in the supplement Fig. S4 reveals that the increase in snow number concentrations can reach

669    up to 2 orders of magnitude during the NW case. This is a logical consequence of the increase

670    in number concentration of ice crystals, which are converting to snow particles after ice crystal

671    growth (i.e., cloud-ice-to-snow autoconversion), when surpassing a characteristic mean

672    diameter of 250 μm. This will be discussed in detail in the following section. Since TAKAHrim

673    and PHILL provide comparable results in terms of the in-cloud phase partitioning, we focus

674    subsequent discussion on the PHILL simulation because it offers the opportunity to explore the

675    sensitivity of simulation results to parameters not considered by the Takahashi formulation.

676

677    *3.1.1 Conditions favoring BR in the two considered events*

678    The temporal evolution of the vertical profiles of $N_{isg}$, IWC and LWC can provide valuable

679    insight on the drivers of enhanced ice formation in the wintertime alpine MPCs. Fig. 5 reveals

680    the presence of a seeder-feeder cloud system with sustained mixed-phase conditions confined

681    to levels below ~3 km (~1.5 km) in the NW (SE) case and a pure ice cloud aloft. Such

682    configurations are a well-known type of orographic multi-layer clouds that enhances

683    precipitation over mountains (e.g., Browning et al., 1974, 1975; Roe, 2005). Cloud

684    condensation is promoted by the synergy between a midlatitude frontal system and its

685    orographically induced ascent over the mountain range (Fig. 1). The separation between the

686    seeder and feeder clouds is often nonexistent, meaning that ice seeding can occur either in

687    layered clouds or internally within one cloud (Roe, 2005; Proske et al., 2021). In the first case,

688    which seems to occur here as well, there can be vertical continuum of cloud condensates

689    between the seeder and the feeder cloud due to precipitation of ice crystals from the higher-

690    level cloud (Fig. 5a). This means that the seeding ice crystals fall through subsaturated cloud-

691    free air before reaching the feeder region of the cloud and might sublimate. The remote-sensing

692    analysis over Switzerland presented by Proske et al. (2021), showed that in-cloud seeding

693    occurs in 18% of the observations, while the external seeder-feeder mechanism is present 15%

694    of the time when the seeder is a cirrus cloud.

695
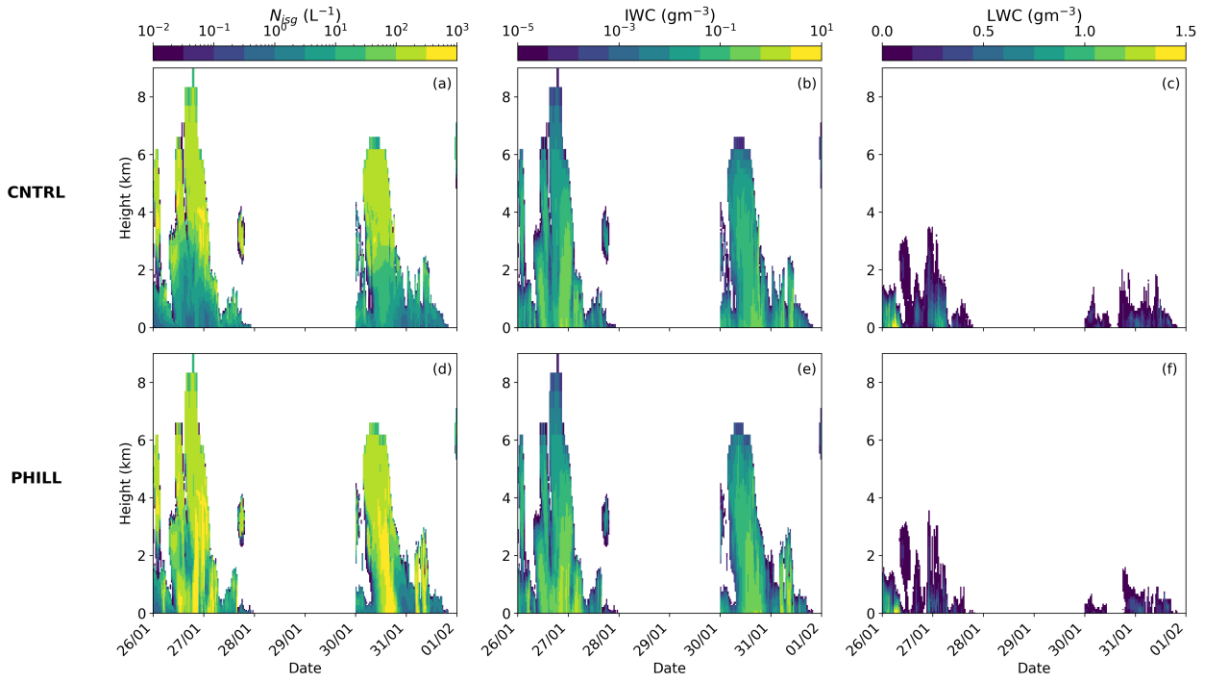
696
697    **Figure 5.** Time-height plots of total $N_{isg}$ (a, d), IWC (b, e) and LWC (c, f) produced by CNTRL
698    (top panel) and PHILL (bottom panel) simulations between 26 January and 1 February 2014.
699    The height is given in km a.g.l.

700

701    To illustrate the processes taking place during the two cases of interest, Fig. 6 displays

702    the tendency of primary and secondary ice production as well as the growth of ice particles

703    through deposition, riming and aggregation from the CNTRL and PHILL simulations at 17:00

704    (19:00) UTC on 26 (30) January. The vertical profiles on 26 January are taken within the

705    seeder-feeder event, while those on 30 January are taken when the high-level cloud associated

706    with the warm front has already passed the region of interest. Upon arrival of the frontal system

707    on 26 January, CNTRL indicates a rapid increase of the total $N_{isg}$ near cloud top (Fig. 5a), which

708    is not shown in the vertical profile of primary ice production rates taken at 17:00 UTC (Fig.

709    6a). The ice particles consisting the seeder cloud are, therefore, formed far from the JFJ station

710    and seem to be advected over the domain of interest. Primary ice crystals are formed in both

711    cases below 2 km in the feeder cloud at temperatures lower than -30 °C through heterogeneous

712    freezing (Fig. 6a). At these heights supercooled liquid water is also present (Fig. 5c) and the

713    newly formed ice particles start growing initially by vapor deposition due to supersaturation

714  with respect to ice, followed by riming (Fig. 6b). This is also indicated by the increased IWC
715  values closer to the ground (Fig. 5b).

716
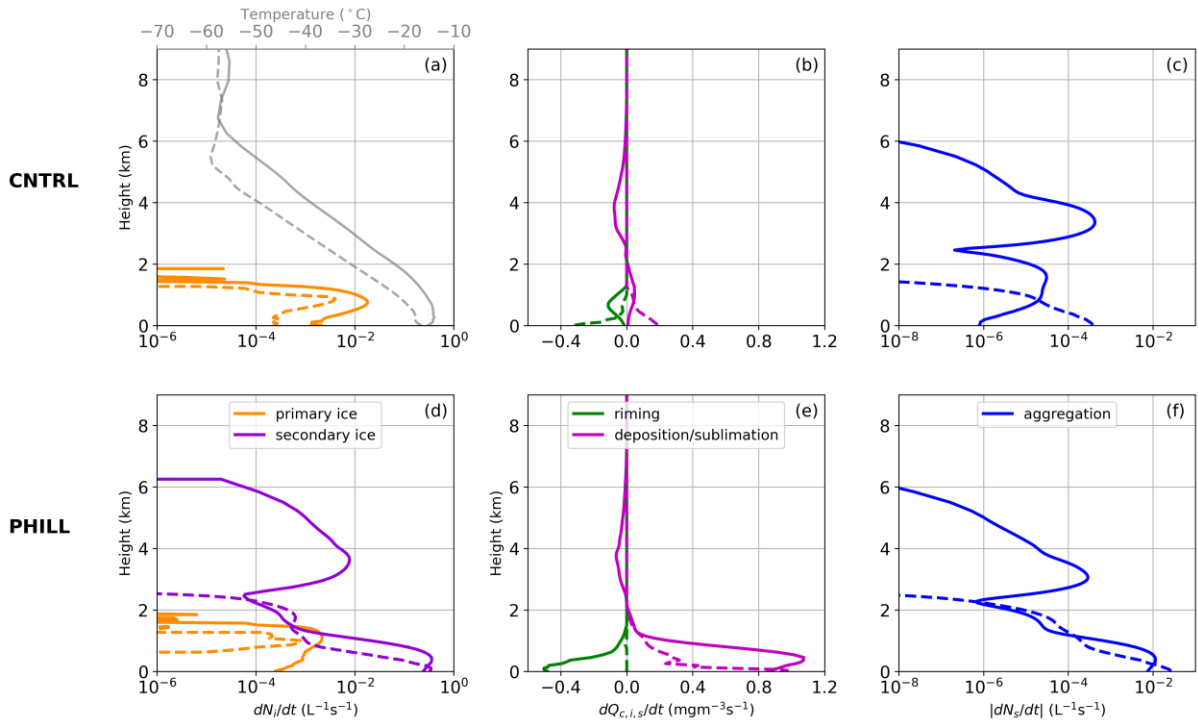
717

718  **Figure 6.** Vertical profiles of (a, d) primary and secondary ice production, (b, e) riming and
719  vapor deposition or sublimation and (c, f) snow aggregation produced by the CNTRL (top
720  panel) and PHILL (bottom panel) simulations at 17:00 UTC on 26 January (solid line) and at
721  19:00 UTC on 30 January (dashed line). The vertical profile of simulated temperature is also
722  superimposed in (a). The cloud liquid water content ($Q_c$) is shown in panels (b and e) to
723  represent the tendency due to riming, while the mass mixing ratio of the ice and snow species
724  ($Q_i + Q_s$), are representing the relative tendencies due to vapor deposition or sublimation. Note
725  that the tendencies due to snow aggregation in (c, f) are presented in absolute values. The height
726  is given in km a.g.l.

727

728      Focusing on the ice-seeding event of 26 January, the enhanced aggregation rate observed
729  at heights above ~2.5 km in the atmosphere indicates the enhanced collision efficiencies of
730  precipitating ice particles while falling from the seeder cloud (Fig. 6c). Note that a portion of
731  the sedimented ice particles sublimates before reaching the feeder cloud at heights ~3-5 km,
732  indicating the prevailing unsaturated conditions in this layer (Fig. 6b). Within this layer
733  aggregation of snowflakes weakens, while it is enhanced again when the falling hydrometeors
734  enter the feeder cloud. The bottom line is that, even under the simulated seeder-feeder events
735  the concentrations of ice particles reaching the ground in CNTRL remain severely
736  underestimated (Section 3.1). Despite the low concentrations of ice crystals simulated by the
737  CNTRL simulation, the low-level cloud is glaciated more frequently during the SE- than during

738  the NW-winds case (Fig. 5c). This is probably because of the higher updraft velocities
739  prevailing until 28 January (Fig. 2d), preventing ice crystals from falling through the lower
740  parts of the cloud (Lohmann et al., 2016).

741      Activating the BR mechanism along with the seeding of precipitating hydrometeors in
742  PHILL shifts the simulated $N_{isg}$ towards higher concentrations that are found to exceed 300 L$^{-1}$
743  in the lower-level part of the cloud (Fig. 5d). On 26 January the mode of the cloud ice
744  distribution shifts to slightly bigger sizes, while on 30 January the modal sizes become almost
745  an order of magnitude smaller compared with the CNTRL simulation (supplement Fig. S4).
746  The enhanced concentrations of bigger ice particles simulated in the first case experience rapid
747  growth through vapor deposition and riming (Fig. 6e) causing a slight increase in the simulated
748  IWC (Fig. 5e) at the expense of the surrounding cloud droplets in the low-level feeder cloud
749  (Fig. 5f). Nevertheless, the smaller ice particles simulated in the second case grow less
750  efficiently through vapor deposition, while the explosive multiplication of ice through BR
751  seems to fully glaciate the low-level cloud below ~1 km resulting in an almost zero riming rate
752  (Fig. 6e). The reduced primary ice production rate observed during both case studies is a
753  consequence of the depletion of liquid water when BR is considered (Fig. 6d). A suppression
754  of heterogeneous ice nucleation following the introduction of SIP into models has already been
755  reported in previous studies (Phillips et al., 2017b; Dedekind et al., 2021; Zhao and Liu, 2021b).

756      The key difference between CNTRL and PHILL simulations is that the latter takes
757  advantage of the enhanced ice particle growth through aggregation while falling to the feeder
758  cloud below ~2 km, where large snowflakes coexist with smaller ice crystals (Fig. 4a, 6a, 6d).
759  This allows for differential settling, which enhances collision efficiency facilitating ice
760  multiplication through BR. This is the reason why the vertical profile of secondary ice
761  formation agrees with the corresponding profile of aggregation during both case studies (Fig.
762  6d, 6f). On 26 January the first secondary ice particles start forming already within the seeder
763  cloud with the contribution of SIP increasing considerably when reaching the feeder cloud,
764  where the tendency due to SIP is more than 3 orders of magnitude higher than primary ice
765  production (Fig. 6d). The significant role of SIP stands out also on 30 January at altitudes below
766  2 km. It is, therefore, essential to consider SIP though BR in the feeder cloud, in order to
767  achieve the enhanced levels of ICNCs frequently observed within seeder-feeder events in the
768  alpine region. This is in agreement with the observational study of Ramelli et al. (2021) on an
769  ice-seeding case occurring in the region around Davos in the Swiss Alps. In this study, they
770  proposed that SIP though HM and BR were necessary to explain the elevated ICNCs in feeder
771  clouds.

772     A classification of the dominant type of precipitation was applied to the polarimetric data

773     collected by a weather radar deployed at the Kleine Scheidegg station (2061 m a.s.l) during the

774     SE case between 30 and 31 January (supplement Fig. S6). In the derived time series, we can

775     identify periods when individual ice crystals (not aggregated and not significantly rimed)

776     dominate over the entire precipitation column followed by periods when a clear stratification

777     is present with ice crystals aloft and mostly aggregates and rimed ice particles below. This

778     stratification is observed on 30 January at 19:00 UTC when the model tendencies are extracted

779     (dashed lines in Fig. 6). Allowing for the BR process in PHILL results in a 2 orders of

780     magnitude enhancement in the aggregation rates close to the ground, which can better

781     reproduce the signatures observed in the hydrometeor classification at that time. An increase

782     in the simulated aggregates and rimed particles is expected to increase orographic precipitation,

783     which is important given that these low-level feeder clouds are incapable of producing

784     significant amounts of precipitation. Indeed, the mean surface precipitation produced by

785     PHILL is 30% (10%) increased during the NW (SE) case compared with CNTRL (supplement

786     Fig. S7), which is in contrast to Dedekind et al. (2021) where the activation of the BR process

787     is found to suppress the regions of strong surface precipitation. This was attributed to the

788     limited efficiency of the small secondary ice particles to grow sufficiently to precipitation sizes

789     when the local updrafts lift them to the upper parts of the cloud that were glaciated. The radar-

790     based hydrometeor classification reveals also the predominance of ice crystals at the beginning

791     and the end of the precipitating periods (e.g., on 30 January at 15:00-17:30 or 31 January at

792     04:30-06:00), which is again more consistent with the vertical profile of $N_i$ produced by PHILL

793     rather than the CNTRL simulation (supplement Fig. S6, S8).

794

795     3.2 Sensitivity to the injection of ice crystals from the surface

796     In this section we examine if the surface-originating small ice particles could have the potential

797     to initiate and enhance ice particle growth in the near-surface MPCs present in our case studies.

798     Fig. 7 illustrates two additional WRF simulations – BIPS10 and BIPS100 – where the ice

799     crystal source applied to the first model level is equal to 10 and 100 $L^{-1}$, respectively (Table 2).

800     Note that these two sensitivity tests do not consider any SIP process to analyze the influence

801     of BIPS only. The total $N_{isg}$ values produced in BIPS10 are only slightly increased compared

802     to the CNTRL simulation and generally remain outside the observed range at JFJ (Fig. 7a). An

803     order of magnitude increase in the applied NBIPS is seen to enhance the modeled $N_{isg}$ during

804     both case studies, however our simulations are still lacking ice particles. This is particularly

805     evident during the NW winds case, where the simulated $N_{isg}$ varies most of the time around 10

806    L$^{-1}$, remaining an order of magnitude lower than the observations. During the SE case, the
807    model performance is slightly improved with the $N_{isg}$ reaching up to ~25 L$^{-1}$ in BIPS100, which
808    occasionally falls within the lower limit of the observed ICNC values (e.g., in the evening of
809    31 January). At times when the detected ICNCs remain quite low (i.e., on the order of 10 L$^{-1}$),
810    the contribution of blowing snow particles probably from the Aletsch Glacier is sufficient to
811    explain the observations at JFJ.

812
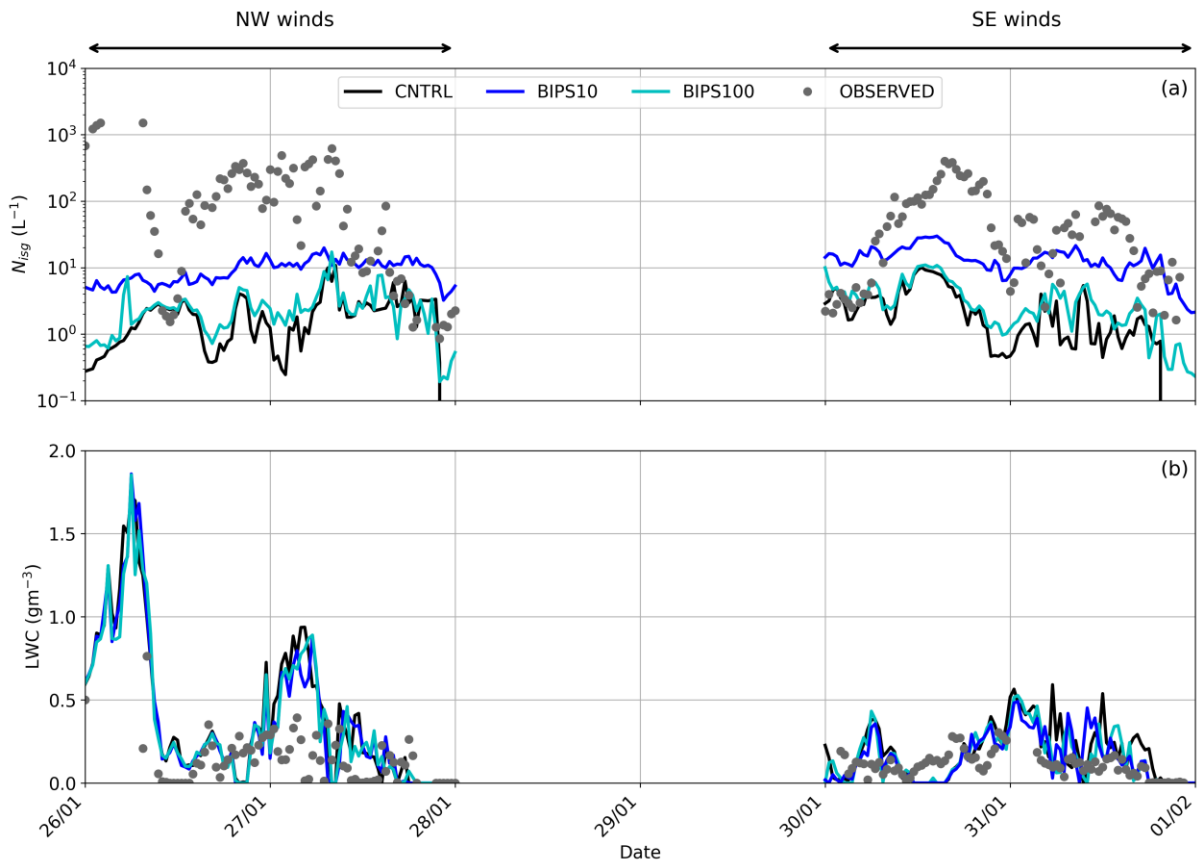
813
814    **Figure 7.** Time series of (a) total $N_{isg}$ and (b) LWC, predicted between 26 January and 1
815    February 2014 by the two sensitivity simulations accounting for the effect of blowing snow,
816    BIPS10 (cyan line) and BIPS100 (blue line).

817

818          As indicated in Fig. 7b, during the NW flow the simulated LWC at the first model level
819    in BIPS10 and BIPS100 almost coincides with the CNTRL simulation of WRF. The three
820    sensitivity simulations are producing comparable median and quartile LWC values (Table 5),
821    with BIPS10 and BIPS100 producing median LWC values closer to the observed ones during
822    the SE flow. When comparing against the LWC values in the third quartile though, the two
823    simulations lead to an overestimation up to a factor of ~1.5 during both case studies. Given that
824    there is approximately a factor of >20 (5) difference between the modeled and observed ICNCs

825    during the NW (SE) winds case (Table 3), Fig. 7 overall reveals that the addition of a source

826    of ice crystals from the effect of blowing snow cannot account for the observed liquid-ice phase

827    partitioning in the simulated orographic MPCs.

828          Our findings are in contrast with the modeling study of Farrington et al. (2016), where a

829    different approach was proposed to include the surface effect on the ICNCs simulated with

830    WRF. In this study, a single model domain was used with a horizontal resolution of 1 km. To

831    account for the flux of hoar crystals being detached from the surface by mechanical fracturing,

832    Farrington et al. (2016) included a wind-dependent surface flux of frost flowers adapted from

833    Xu et al. (2013). Despite the improved performance of WRF in terms of predicted ICNCs and

834    LWC, the wind-dependent formulation of the surface flux caused the modeled ICNCs to

835    become strongly correlated with the simulated horizontal wind speed – a behavior that was not

836    confirmed by the observations of Lloyd et al. (2015). Nonetheless, the highest observed ICNCs

837    at the beginning of the NW case correspond to the time when both the observed and modeled

838    wind speed is the strongest (Fig. 2c), implying that a wind-dependent surface flux of BIPS

839    could potentially elevate the simulated $N_{isg}$ to the observed levels at this time.

840

841    3.3 The synergistic impact of BR and surface-induced ice crystals

842    It is deducible from the above discussion that the sole inclusion of a constant source of BIPS

843    in our simulations cannot efficiently bridge the gap between modeled and measured ICNCs.

844    Our aim in this section is to explore the combined effect of SIP through BR and blowing snow

845    on the simulated orographic MPCs, since both processes are deemed to be important when

846    trying to explain the high ICNCs observed in alpine environments. This is addressed in the

847    final sensitivity simulation, BIPS100_PHILL, the results of which are compared with the

848    CNTRL and PHILL simulations in Fig. 8.

849          In terms of the modeled ice particle concentrations, the combination of the simplified

850    blowing snow treatment and BR parameterization can account for most of the discrepancy

851    between modeled and observed ICNCs, particularly during the SE case (Fig. 8a), when the

852    simulation leads to best agreement with the observed interquartile values (Table 3).

853    BIPS100_PHILL and CNTRL generally differ by an average factor of ~100 (40) during the

854    NW (SE) case, with the former producing $N_{isg}$ values that are sometimes elevated by up to ~3

855    (2) orders of magnitude (Fig. 8a). Compared to the PHILL setup, including a source of BIPS

856    is found to improve the modeled ICNCs close to the surface episodically – for instance in the

857    evening of 30 and 31 January, with the $N_{isg}$ in BIPS100_PHILL efficiently reaching the

858 observed levels (Fig. 8a). Note that BIPS can contribute to the modeled $N_{isg}$ even without the
859 presence of a near-surface orographic cloud (e.g., Geerts et al., 2015; Beck et al., 2018). For
860 instance, BIPS100_PHILL is the only sensitivity simulation producing high $N_{isg}$ values in the
861 evening of 27 and 31 January, when the low-level cloud is dissipated (Fig. 5c, f). In the former
862 case, however, the model results in an overestimate of the ICNCs, which is also observed
863 during the early hours of 30 January, suggesting that the applied source of ice crystals is
864 unrealistically high at this time.
865
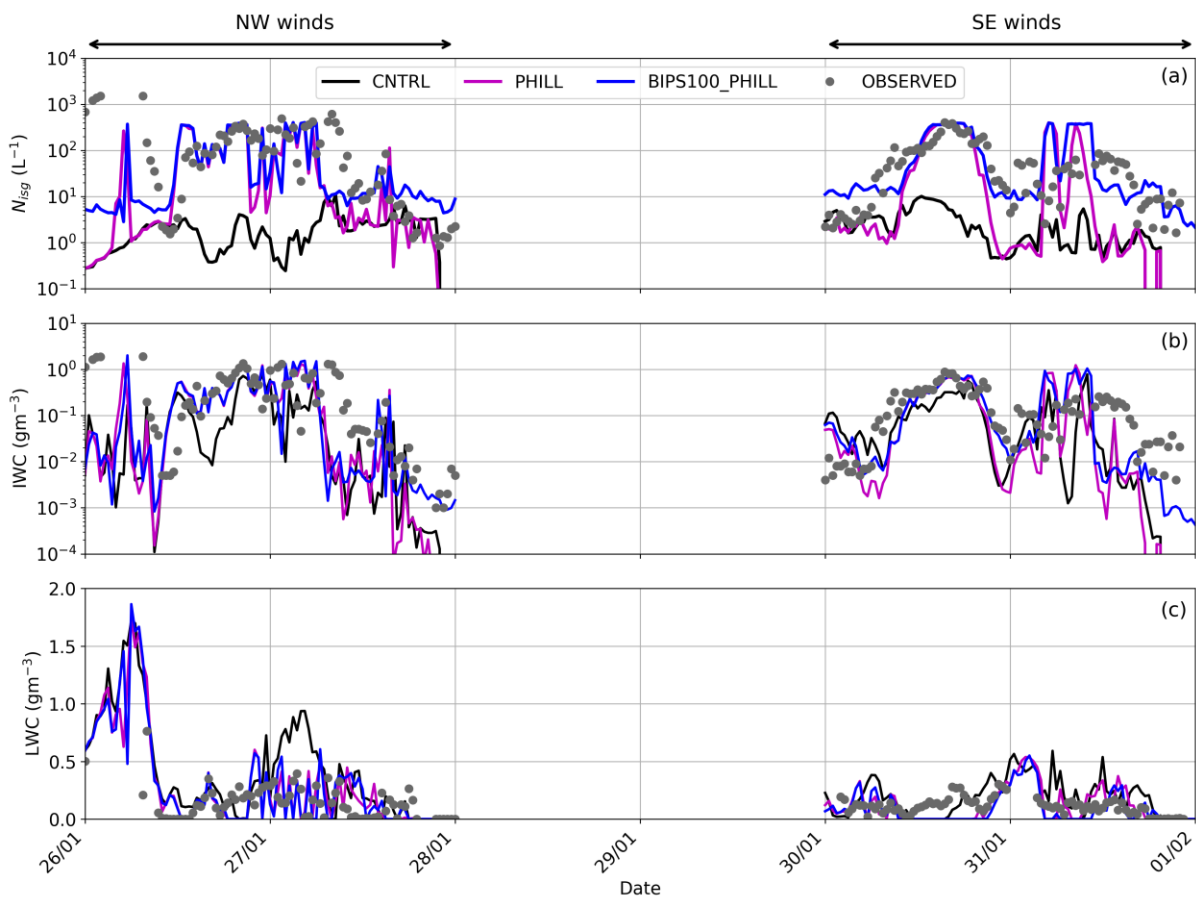
866
867 **Figure 8.** Time series of (a) total $N_{isg}$, (b) IWC and (c) LWC, predicted between 26 January
868 and 1 February 2014 by the sensitivity simulation BIPS100_PHILL (blue line), which
869 examines the combined effect of ice multiplication through BR and blowing snow.
870

871     As the mixed-phase conditions are sustained throughout both case studies (Fig. 8c), the
872 plume of ice crystals is mixed into an ice-supersaturated environment and, thus, BIPS are
873 expected to promote ice growth through their interaction with the surrounding supercooled
874 liquid droplets and (ice) supersaturated air. The number of BIPS reaching the cloud base might
875 not be large, but their presence is expected to further facilitate the action of the BR mechanism,
876 considering the depositional growth they will undergo within the supercooled boundary layer

877    cloud. This is illustrated for example with the concurrent increase in $N_{isg}$ and IWC observed on
878    30 January at approximately 21:00 UTC (Fig. 8a, 8b) in the presence of the low-level cloud
879    (Fig. 8c). Note that the elevated $N_{isg}$ caused by the addition of BIPS is not always followed by
880    an efficient increase in the simulated IWC. This can be observed for example on 27 January at
881    12:00 UTC or in the evening of 31 January (Fig. 8b).

882        A discrepancy between modeled and observed IWC was also highlighted in the study of
883    Farrington et al. (2016), and was attributed to the small sizes of the hoar frost particles assumed
884    (i.e., 10 μm). Although here BIPS are assumed to have sizes of 100 μm, still the
885    underestimation in the cloud IWC has not been overcome. This suggests that the applied source
886    of BIPS combined with the effect of SIP through BR shifts the ice particle spectra to smaller
887    sizes, which are not very efficient in riming and the WBF process and, thus, do not always
888    contribute to significant increases in IWC values. Overall, the interquartile values presented in
889    Table 4 reveal that BIPS100_PHILL and PHILL yield almost identical IWC values, suggesting
890    that the implementation of a constant source of BIPS does not further improve the
891    representation of the total ice mass despite the improvements in the simulated $N_{isg}$. Focusing
892    on the LWC values in the third quartile, though, including a source of BIPS results in better
893    agreement with the CLACE observations during the SE case, while it is shown to have little
894    effect on the cloud liquid phase during the NW case (Table 5). Despite the increase in the
895    modeled $N_{isg}$ observed in BIPS100_PHILL especially during the SE case, the liquid water in
896    the low-level orographic cloud is not further depleted (Fig. 8c). This is presumably because the
897    mean surface precipitation produced is also enhanced by almost ~20% compared to PHILL
898    (supplement Fig. S7), which seems to balance the excessive ice production.

899        One final point that is worth noting here is that there are still some certain periods when
900    BIPS100_PHILL fails to reproduce the observed range of ICNCs. This could imply the
901    potential contribution of additional ice multiplication processes to the observed ice particle
902    concentrations. Indeed, the seeder-feeder configuration observed in the examined case studies
903    could favor the fragmentation of sublimating hydrometeors while falling through an
904    subsaturated environment before entering the feeder cloud (e.g., Bacon et al., 1998). The so-
905    called "sublimational break-up" is an overlooked SIP process which is not yet described in the
906    M05 scheme. Also, note that the periods when the modeled ICNCs remain below the observed
907    ice number levels are mainly identified when the simulated temperature drops below –15 ºC
908    and the wind speed exceeds 10 ms$^{-1}$ or even 20 ms$^{-1}$ (e.g., in the morning of 26 January or 27
909    January at around 12:00 UTC). This is when the incorporation of surface-based processes
910    becomes of primary importance. The simplified methodology we followed here although

instructive, yet it faces several limitations. For instance, the constant source of BIPS is sometimes found to overestimate the modeled $N_{isg}$ and IWC. In order to accurately assess the potential role of the snow-covered surfaces in elevating the simulated ICNCs, an improved spatio-temporal description of the concentration and distribution of BIPS is required. Furthermore, the applied ice crystal source is independent of some key parameters controlling its resuspension, such as the horizontal wind speed, the updrafts or the friction velocity (e.g., Vionnet et al., 2013, 2014). For example, in the early morning hours of 26 January, the high simulated horizontal and vertical velocities (Fig. 2c, 2d) are expected to loft significant BIPS concentrations into the cloud layer, owing to enhanced mechanical mixing and momentum flux close to the surface. Nonetheless, the contribution of the induced plume of BIPS remains constant throughout the NW case study (Fig. 7a), which seems to lead to an underestimation of the total ice particle concentration and mass. A more realistic parameterization of the BIPS flux or the coupling with a detailed snowpack model would, therefore, be essential for a more accurate representation of the effect of blowing snow.

## 4.    Summary and conclusions

This study employs the mesoscale model WRF to explore the potential impact of ice multiplication processes on the liquid-ice phase partitioning in the orographic MPCs observed during the CLACE 2014 campaign at the mountain-top site of JFJ in the Swiss Alps. The orography surrounding JFJ channels the direction of the horizontal wind speed, giving us the opportunity to analyze two frontal cases occurring under NW and SE conditions.

DS and BR mechanisms were implemented in the default M05 scheme in WRF, in addition to the HM parameterization, which however remained inactive in the simulated temperature range (–10 to –24 °C). The DS process is parameterized following either the latest theoretical formulation developed by Phillips et al. (2018) or the more simplified parameterization proposed by Sullivan et al. (2018a). Our sensitivity simulations revealed that the DS mechanism is ineffective in the two considered alpine MPCs, even under the higher updraft velocity conditions associated with the NW winds case study, owing to the lack of large drops required for the process.

To parameterize the number of fragments generated per ice-ice collision we followed again two different approaches: either the simplified temperature dependent formulation of Takahashi et al. (1995) scaled for the size of the particle that undergo fragmentation

943    (Sotiropoulou et al., 2021a) or the more advanced physically-based Phillips et al. (2017a)

944    parameterization. It is important to apply the Takahashi parameterization only to consider

945    collisions between rimed ice particles, otherwise the number of generated fragments is

946    significantly overestimated. Including a description of the BR mechanism is essential for

947    reproducing the ICNCs observed in the simulated orographic clouds, especially at temperatures

948    higher than ~ $-15\ ^{\circ}$C, where INPs are generally sparse. SIP through BR is found to enhance the

949    modeled ICNCs by up to 3 (2) orders of magnitude during the NW (SE) case, improving the

950    model agreement with observations. This ice enhancement can cause up to an order of

951    magnitude increase in the mean simulated IWC values compared with the CNTRL simulation,

952    which is attributed to the enhanced ice crystal growth and cloud-ice-to-snow autoconversion.

953    The increase in the simulated ICNCs also depletes the cloud LWC by at least a factor of 2

954    during both cases, which is more consistent with the measured LWC values.

955        One of the most interesting outcomes of this study is the association of the enhanced BR

956    efficiency with the occurrence of in-cloud seeder-feeder events, which are commonly found in

957    Switzerland (Proske et al., 2021). While ice-seeding situations are associated with enhanced

958    orographic precipitation in the alpine region, the CNTRL simulation fails to reproduce the

959    elevated ICNCs reaching the ground. The falling ice hydrometeors experience efficient growth

960    through aggregation in the seeder part of the cloud, which is enhanced when reaching the feeder

961    cloud at altitudes below 2 km, where primary ice crystals form and grow through vapor

962    deposition and riming. Aggregation of snowflakes seems to be the major driver of secondary

963    ice formation in the examined seeder-feeder events. SIP though BR is initiated already within

964    the seeder cloud, while it becomes immensely important in the feeder cloud where its

965    production rate exceeds the one of primary ice formation. The increased generation of

966    secondary ice fragments does not always lead to ice explosion and cloud glaciation, as it is

967    followed by an enhancement in the precipitation sink owing to a shift in the ice particle

968    spectrum. Including a description of the BR mechanism is, therefore, crucial for explaining the

969    ice particle concentration and mass observed in the low-level feeder clouds.

970        To assess the potential role of blowing snow in the simulated orographic clouds, a

971    constant source of ice crystals was introduced in the first atmospheric level of WRF. Our results

972    indicate that blowing snow alone cannot explain the high ICNCs observed at JFJ, but when this

973    source is combined with the BR mechanism then the gap between modeled and measured

974    ICNCs is sufficiently bridged. The biggest influence of blowing snow is mainly detected at

975    times when the simulated temperatures are low enough ($< -15\ ^{\circ}$C), while the presence of a low-

976 level cloud is required for SIP to manifest. The concentrations of BIPS reaching the cloud base

977 are not high, but when they are mixed among supercooled liquid droplets they are expected to

978 grow, facilitating ice multiplication through BR. Nonetheless, including a wind-dependence or

979 a spatio-temporal variability in the applied ice crystal source would be essential to provide a

980 more precise description of the effect of blowing snow on the simulated clouds.

981    Overall, our findings indicate that outside the HM temperature range, a correct

982 representation of both secondary ice (through BR) and an external ice seeding mechanism,

983 which is primarily precipitating ice particles formed aloft and to a lesser degree wind-blown

984 ice from the surface, is fundamentally important for accurately predicting the liquid-ice

985 partitioning and properties of MPCs. Given the high frequency of seeder-feeder events in

986 orographic environments, including the new physics of BR may address a large source of

987 predictive bias in atmospheric models.

988

989 *Code and data availability.* The WRF outputs and the microphysical observations presented in

990 this  study  can  be  downloaded  from  the  EnviDat  data  portal  at

991 https://doi.org/10.16904/envidat.271 (last access: 13 January 2022; Georgakaki et al., 2022).

992 Meteorological data are downloaded from the Swiss Federal Office of Meteorology and

993 Climatology MeteoSwiss site (https://gate.meteoswiss.ch/idaweb/login.do, Meteosuisse,

994 2022). The updated Morrison scheme is available upon request.

995

996 *Competing interests.* The authors declare no conflict of interest.

997

998 *Author Contributions.* PG and AN conceived and led this study with input from GS. EV helped

999 with the WRF configuration and setup. GS provided the updated microphysics scheme with

1000 the detailed BR parameterizations. PG implemented the DS parameterizations with help from

1001 GS, conducted the simulations, analyzed the results and, together with AN, wrote the main

1002 paper. All authors contributed to the scientific interpretation and writing of the paper.

1003

1004 *Acknowledgements.* The authors would like to thank Gary Lloyd for providing the

1005 microphysical measurements, as well as Jacopo Grazioli for collecting and pre-processing the

1006  radar data. The authors are also thankful to Varun Sharma and Michael Lehning for the fruitful

1007  discussions on the contribution of blowing snow in the alpine region.

1008

1009  *Financial support.* This research has been supported by the Horizon 2020 project FORCeS

1010  (grant 821205) and the European Research Council project PyroTRACH (grant 726165). GS

1011  received funding from the Swedish Research Council for Sustainable Development FORMAS

1012  (project ID 2018-01760). GS and AN acknowledge support by the European Union under the

1013  H2020 Marie Skłodowska-Curie Actions project SIMPHAC under grant agreement 898568.

**References**

Atlas, R. L., Bretherton, C. S., Blossey, P. N., Gettelman, A., Bardeen, C., Lin, P. and Ming, Y.: How Well Do Large-Eddy Simulations and Global Climate Models Represent Observed Boundary Layer Structures and Low Clouds Over the Summertime Southern Ocean?, J. Adv. Model. Earth Syst., 12(11), 1–25, doi:10.1029/2020MS002205, 2020.

Baltensperger, U., Schwikowski, M., Jost, D. T., Nyeki, S., Gäggeler, H. W. and Poulida, O.: Scavenging of atmospheric constituents in mixed phase clouds at the high-alpine site Jungfraujoch part I: Basic concept and aerosol scavenging by clouds, Atmos. Environ., 32, 3975–3983, doi:10.1016/S1352-2310(98)00051-X, 1998.

Beck, A., Henneberger, J., Fugal, J. P., David, R. O., Lacher, L. and Lohmann, U.: Impact of surface and near-surface processes on ice crystal concentrations measured at mountain-top research stations, Atmos. Chem. Phys., 18(12), 8909–8927, doi:10.5194/acp-18-8909-2018, 2018.

Beheng, K. D.: Microphysical Properties of Glaciating Cumulus Clouds: Comparison of Measurements With A Numerical Simulation, Q. J. R. Meteorol. Soc., 113(478), 1377–1382, doi:10.1002/qj.49711347815, 1987.

Bergeron, T.: On the physics of clouds and precipitation, Proc. 5th Assembly UGGI, 1935, Lisbon, Portugal, 156–180, 1935.

Bigg, E. K.: The supercooling of water, Proc. Phys. Soc. Sect. B, 66(8), 688–694, doi:10.1088/0370-1301/66/8/309, 1953.

Brown, P. R. A. and Francis, P. N.: Improved Measurements of the Ice Water Content in Cirrus Using a Total-Water Probe, J. Atmos. Ocean. Technol., 12, 410–414, doi:10.1175/1520-0426(1995)012<0410:IMOTIW>2.0.CO;2, 1995.

Browning, K. A., Hill, F. F. and Pardoe, C. W.: Structure and mechanism of precipitation and the effect of orography in a wintertime warm sector, Q. J. R. Meteorol. Soc., 100(425), 309–330, doi:10.1002/qj.49710042505, 1974.

Browning, K. A., Pardoe, C. W. and Hill, F. F.: The nature of orographic rain at wintertime cold fronts, Q. J. R. Meteorol. Soc., 101(428), 333–352, doi:10.1002/qj.49710142815, 1975.

Chen, F. and Dudhia, J.: Coupling and advanced land surface-hydrology model with the Penn State-NCAR MM5 modeling system. Part I: Model implementation and sensitivity, Mon. Weather Rev., 129(4), 569–585, doi:10.1175/1520-0493(2001)129<0569:CAALSH>2.0.CO;2, 2001.

1047    Chou, C., Stetzer, O., Weingartner, E., Jurányi, Z., Kanji, Z. A. and Lohmann, U.: Ice nuclei
1048        properties within a Saharan dust event at the Jungfraujoch in the Swiss Alps, Atmos.
1049        Chem. Phys., 11, 4725–4738, doi:10.5194/acp-11-4725-2011, 2011.

1050    Choularton, T. W., Griggs, D. J., Humood, B. Y. and Latham, J.: Laboratory studies of riming,
1051        and its relation to ice splinter production, Q. J. R. Meteorol. Soc., 106(448), 367–374,
1052        doi:10.1002/qj.49710644809, 1980.

1053    Choularton, T. W., Bower, K. N., Weingartner, E., Crawford, I., Coe, H., Gallagher, M. W.,
1054        Flynn, M., Crosier, J., Connolly, P., Targino, A., Alfarra, M. R., Baltensperger, U.,
1055        Sjogren, S., Verheggen, B., Cozic, J. and Gysel, M.: The influence of small aerosol
1056        particles on the properties of water and ice clouds, Faraday Discuss., 137, 205–222,
1057        doi:10.1039/b702722m, 2008.

1058    Chow, F. K., De Wekker, Stephan, F. J., and Snyder, B. J.: Mountain weather research and
1059        forecasting: recent progress and current challenges, Springer, Dordrecht, the Netherlands,
1060        2013.

1061    Conen, F., Rodríguez, S., Hüglin, C., Henne, S., Herrmann, E., Bukowiecki, N. and Alewell,
1062        C.: Atmospheric ice nuclei at the high-altitude observatory Jungfraujoch, Switzerland,
1063        Tellus, Ser. B Chem. Phys. Meteorol., 67(1), doi:10.3402/tellusb.v67.25014, 2015.

1064    Cooper, W. A.: Ice initiation in natural clouds, Meteor. Mon., 21, 29–32,
1065        https://doi.org/10.1175/0065-9401-21.43.29, 1986.

1066    Crosier, J., Bower, K. N., Choularton, T. W., Westbrook, C. D., Connolly, P. J., Cui, Z. Q.,
1067        Crawford, I. P., Capes, G. L., Coe, H., Dorsey, J. R., Williams, P. I., Illingworth, A. J.,
1068        Gallagher, M. W. and Blyth, A. M.: Observations of ice multiplication in a weakly
1069        convective cell embedded in supercooled mid-level stratus, Atmos. Chem. Phys., 11(1),
1070        257–273, doi:10.5194/acp-11-257-2011, 2011.

1071    Dedekind, Z., Lauber, A., Ferrachat, S., and Lohmann, U.: Sensitivity of precipitation
1072        formation to secondary ice production in winter orographic mixed-phase clouds, Atmos.
1073        Chem. Phys., 21, 15115–15134, https://doi.org/10.5194/acp-21-15115-2021, 2021.

1074    Déry, S. J. and Yau, M. K.: A climatology of adverse winter-type weather events, J. Geophys.
1075        Res. Atmos., 104(D14), 16657–16672, doi:10.1029/1999JD900158, 1999.

1076    Farrington, R. J., Connolly, P. J., Lloyd, G., Bower, K. N., Flynn, M. J., Gallagher, M. W.,
1077        Field, P. R., Dearden, C. and Choularton, T. W.: Comparing model and measured ice
1078        crystal concentrations in orographic clouds during the INUPIAQ campaign, Atmos. Chem.
1079        Phys., 16(8), 4945–4966, doi:10.5194/acp-16-4945-2016, 2016.

1080    Field, P. R. and Heymsfield, A. J.: Importance of snow to global precipitation, Geophys. Res.

1081       Lett., 42(21), 9512–9520, doi:10.1002/2015GL065497, 2015.

1082 Field, P. R., Lawson, R. P., Brown, P. R. A., Lloyd, G., Westbrook, C., Moisseev, D.,
1083       Miltenberger, A., Nenes, A., Blyth, A., Choularton, T., Connolly, P., Buehl, J., Crosier, J.,
1084       Cui, Z., Dearden, C., DeMott, P., Flossmann, A., Heymsfield, A., Huang, Y., Kalesse, H.,
1085       Kanji, Z. A., Korolev, A., Kirchgaessner, A., Lasher-Trapp, S., Leisner, T., McFarquhar,
1086       G., Phillips, V., Stith, J. and Sullivan, S.: Chapter 7. Secondary Ice Production - current
1087       state of the science and recommendations for the future, Meteorol. Monogr., 58,
1088       doi:10.1175/amsmonographs-d-16-0014.1, 2017.

1089 Findeisen, W.: Die kolloidmeteorologischen vorgänge bei der niederschlagsbildung, Meteorol.
1090       Z., 55, 121–133, 1938.

1091 Fridlind, A. M., Ackerman, A. S., McFarquhar, G., Zhang, G., Poellot, M. R., DeMott, P. J.,
1092       Prenni, A. J. and Heymsfield, A. J.: Ice properties of single-layer stratocumulus during the
1093       Mixed-Phase Arctic Cloud Experiment: 2. Model results, J. Geophys. Res. Atmos.,
1094       112(24), 1–25, doi:10.1029/2007JD008646, 2007.

1095 Fu, S., Deng, X., Shupe, M. D. and Xue, H.: A modelling study of the continuous ice formation
1096       in an autumnal Arctic mixed-phase cloud case, Atmos. Res., 228(March), 77–85,
1097       doi:10.1016/j.atmosres.2019.05.021, 2019.

1098 Geerts, B., Pokharel, B. and Kristovich, D. A. R.: Blowing snow as a natural glaciogenic cloud
1099       seeding mechanism, Mon. Weather Rev., 143(12), 5017–5033, doi:10.1175/MWR-D-15-
1100       0241.1, 2015.

1101 Georgakaki, P., Nenes, A., Sotiropoulou, G.: Data for the publication "Secondary ice
1102       production processes in wintertime alpine mixed-phase clouds", EnviDat, doi:
1103       10.16904/envidat.271, 2022.

1104 Grazioli, J., Lloyd, G., Panziera, L., Hoyle, C. R., Connolly, P. J., Henneberger, J. and Berne,
1105       A.: Polarimetric radar and in situ observations of riming and snowfall microphysics during
1106       CLACE 2014, Atmos. Chem. Phys., 15, 13787–13802, doi:10.5194/acp-15-13787-2015,
1107       2015.

1108 Griggs, D. J. and Choularton, T. W.: Freezing modes of riming droplets with application to ice
1109       splinter production, Q. J. R. Meteorol. Soc., 109(459), 243–253,
1110       doi:10.1002/qj.49710945912, 1983.

1111 Griggs, D. J. and Choularton, T. W.: A laboratory study of secondary ice particle production
1112       by the fragmentation of rime and vapour-grown ice crystals, Q. J. R. Meteorol. Soc.,
1113       112(471), 149–163, doi:10.1256/smsqj.47108, 1986.

1114 Hallett, J. and Mossop, S. C.: Production of secondary ice particles during the riming process,

Nature, 249, 26–28, doi:10.1038/249026a0, 1974.

Harris, L. M. and Durran, D. R.: An Idealized Comparison of One-Way and Two-Way Grid Nesting, Mon. Weather Rev., 138(6), 2174–2187, doi:10.1175/2010MWR3080.1, 2010.

Henneberg, O., Henneberger, J. and Lohmann, U.: Formation and development of orographic mixed-phase clouds, J. Atmos. Sci., 74(11), 3703–3724, doi:10.1175/JAS-D-16-0348.1, 2017.

Hersbach, H., Bell, B., Berrisford, P., Hirahara, S., Horányi, A., Muñoz-Sabater, J., Nicolas, J., Peubey, C., Radu, R., Schepers, D., Simmons, A., Soci, C., Abdalla, S., Abellan, X., Balsamo, G., Bechtold, P., Biavati, G., Bidlot, J., Bonavita, M., De Chiara, G., Dahlgren, P., Dee, D., Diamantakis, M., Dragani, R., Flemming, J., Forbes, R., Fuentes, M., Geer, A., Haimberger, L., Healy, S., Hogan, R. J., Hólm, E., Janisková, M., Keeley, S., Laloyaux, P., Lopez, P., Lupu, C., Radnoti, G., de Rosnay, P., Rozum, I., Vamborg, F., Villaume, S. and Thépaut, J. N.: The ERA5 global reanalysis, Q. J. R. Meteorol. Soc., 146(730), 1999–2049, doi:10.1002/qj.3803, 2020.

Heymsfield, A. J. and Mossop, S. C.: Temperature dependence of secondary ice crystal production during soft hail growth by riming, Q. J. R. Meteorol. Soc., 110(465), 765–770, doi:10.1002/qj.49711046512, 1984.

Heymsfield, A. J., Schmitt, C., Bansemer, A. and Twohy, C. H.: Improved representation of ice particle masses based on observations in natural clouds, J. Atmos. Sci., 67(10), 3303–3318, doi:10.1175/2010JAS3507.1, 2010.

Hoarau, T., Pinty, J. P. and Barthe, C.: A representation of the collisional ice break-up process in the two-moment microphysics LIMA v1.0 scheme of Meso-NH, Geosci. Model Dev., 11(10), 4269–4289, doi:10.5194/gmd-11-4269-2018, 2018.

Hoose, C. and Möhler, O.: Heterogeneous ice nucleation on atmospheric aerosols: A review of results from laboratory experiments., 2012.

James, R. L., Phillips, V. T. J., and Connolly, P. J.: Secondary ice production during the break-up of freezing water drops on impact with ice particles, Atmos. Chem. Phys., 21, 18519–18530, doi:10.5194/acp-21-18519-2021, 2021.

Janjić, Z. I.: Nonsingular Implementation of the Mellor-Yamada Level 2.5 Scheme in the NCEP Meso model, NOAA/NWS/NCEP Off. note 437, 61 pp, 2002.

Ikawa, M. and Saito, K.: Description of a Non-hydrostatic Model Developed at the Forecast Research Department of the MR, MRI Tech. Rep. 28, 238 pp., 1991.

Kanji, Z. A., Ladino, L. A., Wex, H., Boose, Y., Burkert-Kohn, M., Cziczo, D. J. and Krämer, M.: Overview of Ice Nucleating Particles, Meteorol. Monogr., 58, 1.1-1.33,

doi:10.1175/amsmonographs-d-16-0006.1, 2017.

Keinert, A., Spannagel, D., Leisner, T. and Kiselev, A.: Secondary ice production upon freezing of freely falling drizzle droplets, J. Atmos. Sci., 77(8), 2959–2967, doi:10.1175/JAS-D-20-0081.1, 2020.

Ketterer, C., Zieger, P., Bukowiecki, N., Collaud Coen, M., Maier, O., Ruffieux, D. and Weingartner, E.: Investigation of the Planetary Boundary Layer in the Swiss Alps Using Remote Sensing and In Situ Measurements, Boundary-Layer Meteorol., 151(2), 317–334, doi:10.1007/s10546-013-9897-8, 2014.

Kleinheins, J., Kiselev, A., Keinert, A., Kind, M. and Leisner, T.: Thermal imaging of freezing drizzle droplets: pressure release events as a source of secondary ice particles, J. Atmos. Sci., 1–28, doi:10.1175/jas-d-20-0323.1, 2021.

Korolev, A. and Isaac, G.: Phase transformation of mixed-phase clouds, Q. J. R. Meteorol. Soc., 129(587 PART A), 19–38, doi:10.1256/qj.01.203, 2003.

Korolev, A. and Leisner, T.: Review of experimental studies of secondary ice production., 2020.

Korolev, A., McFarquhar, G., Field, P. R., Franklin, C., Lawson, P., Wang, Z., Williams, E., Abel, S. J., Axisa, D., Borrmann, S., Crosier, J., Fugal, J., Krämer, M., Lohmann, U., Schlenczek, O., Schnaiter, M. and Wendisch, M.: Mixed-Phase Clouds: Progress and Challenges, Meteorol. Monogr., 58, 5.1-5.50, doi:10.1175/amsmonographs-d-17-0001.1, 2017.

Korolev, A., Heckman, I., Wolde, M., Ackerman, A. S., Fridlind, A. M., Ladino, L. A., Paul Lawson, R., Milbrandt, J. and Williams, E.: A new look at the environmental conditions favorable to secondary ice production, Atmos. Chem. Phys., 20(3), 1391–1429, doi:10.5194/acp-20-1391-2020, 2020.

Korolev, A. V., Emery, E. F., Strapp, J. W., Cober, S. G., Isaac, G. A., Wasey, M. and Marcotte, D.: Small ice particles in tropospheric clouds: Fact or artifact? Airborne icing instrumentation evaluation experiment, Bull. Am. Meteorol. Soc., 92(8), 967–973, doi:10.1175/2010BAMS3141.1, 2011.

Krinner, G., Derksen, C., Essery, R., Flanner, M., Hagemann, S., Clark, M., Hall, A., Rott, H., Brutel-Vuilmet, C., Kim, H., Ménard, C. B., Mudryk, L., Thackeray, C., Wang, L., Arduini, G., Balsamo, G., Bartlett, P., Boike, J., Boone, A., Chéruy, F., Colin, J., Cuntz, M., Dai, Y., Decharme, B., Derry, J., Ducharne, A., Dutra, E., Fang, X., Fierz, C., Ghattas, J., Gusev, Y., Haverd, V., Kontu, A., Lafaysse, M., Law, R., Lawrence, D., Li, W., Marke, T., Marks, D., Ménégoz, M., Nasonova, O., Nitta, T., Niwano, M., Pomeroy, J., Raleigh,

M. S., Schaedler, G., Semenov, V., Smirnova, T. G., Stacke, T., Strasser, U., Svenson, S., Turkov, D., Wang, T., Wever, N., Yuan, H., Zhou, W., and Zhu, D.: ESM-SnowMIP: assessing snow models and quantifying snow-related climate feedbacks, Geosci. Model Dev., 11, 5027–5049, https://doi.org/10.5194/gmd-11-5027-2018, 2018.

Lance, S., Brock, C. A., Rogers, D. and Gordon, J. A.: Water droplet calibration of the Cloud Droplet Probe (CDP) and in-flight performance in liquid, ice and mixed-phase clouds during ARCPAC, Atmos. Meas. Tech., 3(6), 1683–1706, doi:10.5194/amt-3-1683-2010, 2010.

Latham, J. and Warwicker, R.: Charge transfer accompanying the splashing of supercooled raindrops on hailstones, Q. J. R. Meteorol. Soc., 106(449), 559–568, doi:10.1002/qj.49710644912, 1980.

Lauber, A., Kiselev, A., Pander, T., Handmann, P. and Leisner, T.: Secondary ice formation during freezing of levitated droplets, J. Atmos. Sci., 75(8), 2815–2826, doi:10.1175/JAS-D-18-0052.1, 2018.

Lauber, A., Henneberger, J., Mignani, C., Ramelli, F., Pasquier, J. T., Wieder, J., Hervo, M. and Lohmann, U.: Continuous secondary-ice production initiated by updrafts through the melting layer in mountainous regions, Atmos. Chem. Phys., 21(5), 3855–3870, doi:10.5194/acp-21-3855-2021, 2021.

Lawson, R. P., O'Connor, D., Zmarzly, P., Weaver, K., Baker, B., Mo, Q. and Jonsson, H.: The 2D-S (stereo) probe: Design and preliminary tests of a new airborne, high-speed, high-resolution particle imaging probe, J. Atmos. Ocean. Technol., 23(11), 1462–1477, doi:10.1175/JTECH1927.1, 2006.

Lawson, R. P., Woods, S. and Morrison, H.: The microphysics of ice and precipitation development in tropical cumulus clouds, J. Atmos. Sci., 72(6), 2429–2445, doi:10.1175/JAS-D-14-0274.1, 2015.

Lehning, M., I.Volksch, D.Gustafsson, Nguyen, T. A., Stahli, M. and Zappa, M.: ALPINE3D: A detailed model of mountain surface processes and its application to snow hydrology., Hydrol. Process., 20, 2111–2128, doi:10.1002/hyp.6204, 2006.

Leisner, T., Pander, T., Handmann, P., and Kiselev, A.: Secondary ice processes upon heterogeneous freezing of cloud droplets, 14th Conf. on Cloud Physics and Atmospheric Radiation, Amer. Meteor. Soc, Boston, MA, 7 July 2014, available at: https://ams.confex.com/ams/14CLOUD14ATRAD/webprogram/Paper250221.html (last access: 9 November 2019), 2014.

Lloyd, G., Choularton, T. W., Bower, K. N., Gallagher, M. W., Connolly, P. J., Flynn, M.,

Farrington, R., Crosier, J., Schlenczek, O., Fugal, J. and Henneberger, J.: The origins of ice crystals measured in mixed-phase clouds at the high-alpine site Jungfraujoch, Atmos. Chem. Phys., 15(22), 12953–12969, doi:10.5194/acp-15-12953-2015, 2015.

Lohmann, U., Henneberger, J., Henneberg, O., Fugal, J. P., Bühl, J. and Kanji, Z. A.: Persistence of orographic mixed-phase clouds, Geophys. Res. Lett., 43(19), 10,512-10,519, doi:10.1002/2016GL071036, 2016.

Lowenthal, D. H., Hallar, A. G., David, R. O., Mccubbin, I. B., Borys, R. D. and Mace, G. G.: Mixed-phase orographic cloud microphysics during StormVEx and IFRACS, Atmos. Chem. Phys., 19(8), 5387–5401, doi:10.5194/acp-19-5387-2019, 2019.

Luke, E. P., Yang, F., Kollias, P., Vogelmann, A. M. and Maahn, M.: New insights into ice multiplication using remote-sensing observations of slightly supercooled mixed-phase clouds in the Arctic, Proc. Natl. Acad. Sci. U. S. A., 118(13), 1–9, doi:10.1073/pnas.2021387118, 2021.

Mahesh, A., Eager, R., Campbell, J. R. and Spinhirne, J. D.: Observations of blowing snow at the South Pole, J. Geophys. Res. Atmos., 108(22), 1–9, doi:10.1029/2002jd003327, 2003.

Meyers, M. P., DeMott, P. J. and Cotton, W. R.: New Primary Ice-Nucleation Parameterizations in an Explicit Cloud Model, J. Appl. Meteorol., 31, 708–721, doi:10.1175/1520- 0450(1992)031<0708:NPINPI>2.0.CO;2, 1992.

Mignani, C., Creamean, J. M., Zimmermann, L., Alewell, C. and Conen, F.: New type of evidence for secondary ice formation at around -15 °c in mixed-phase clouds, Atmos. Chem. Phys., 19(2), 877–886, doi:10.5194/acp-19-877-2019, 2019.

Morrison, H., Curry, J. A. and Khvorostyanov, V. I.: A new double-moment microphysics parameterization for application in cloud and climate models. Part I: Description, J. Atmos. Sci., 62, 1678–1693, doi:10.1175/JAS3446.1, 2005.

Morrison, H. and Grabowski, W. W.: A novel approach for representing ice microphysics in models: Description and tests using a kinematic framework, J. Atmos. Sci., 65(5), doi:10.1175/2007JAS2491.1, 2008.

Morrison, H., De Boer, G., Feingold, G., Harrington, J., Shupe, M. D. and Sulia, K.: Resilience of persistent Arctic mixed-phase clouds, Nat. Geosci., 5(1), 11–17, doi:10.1038/ngeo1332, 2012.

Mott, R., Scipión, D., Schneebeli, M., Dawes, N., Berne, A. and Lehning, M.: Orographic effects on snow deposition patterns in mountainous terrain, J. Geophys. Res., 119(3), 1419–1439, doi:10.1002/2013JD019880, 2014.

Mülmenstädt, J., Sourdeval, O., Delanoë, J. and Quaas, J.: Frequency of occurrence of rain

from liquid-, mixed-, and ice-phase clouds derived from A-Train satellite retrievals, Geophys. Res. Lett., 42(15), 6502–6509, doi:10.1002/2015GL064604, 2015.

Panziera, L. and Hoskins, B.: Large snowfall events in the south-eastern Alps, Weather, 63(4), 88–93, doi:10.1002/wea.178, 2008.

Phillips, V. T. J., Blyth, A. M., Brown, P. R. A., Choularton, T. W. and Latham, J.: The glaciation of a cumulus cloud over New Mexico, Q. J. R. Meteorol. Soc., 127(575), 1513–1534, doi:10.1256/smsqj.57502, 2001.

Phillips, V. T. J., Yano, J. I. and Khain, A.: Ice multiplication by breakup in ice-ice collisions. Part I: Theoretical formulation, J. Atmos. Sci., 74(6), 1705–1719, doi:10.1175/JAS-D-16-0224.1, 2017a.

Phillips, V. T. J., Yano, J. I., Formenton, M., Ilotoviz, E., Kanawade, V., Kudzotsa, I., Sun, J., Bansemer, A., Detwiler, A. G., Khain, A. and Tessendorf, S. A.: Ice multiplication by breakup in ice-ice collisions. Part II: Numerical simulations, J. Atmos. Sci., 74(9), 2789–2811, doi:10.1175/JAS-D-16-0223.1, 2017b.

Phillips, V. T. J., Patade, S., Gutierrez, J. and Bansemer, A.: Secondary ice production by fragmentation of freezing drops: Formulation and theory, J. Atmos. Sci., 75(9), 3031–3070, doi:10.1175/JAS-D-17-0190.1, 2018.

Proske, U., Bessenbacher, V., Dedekind, Z., Lohmann, U. and Neubauer, D.: How frequent is natural cloud seeding from ice cloud layers ( <-35°C) over Switzerland?, Atmos. Chem. Phys., 21(6), 5195–5216, doi:10.5194/acp-21-5195-2021, 2021.

Pruppacher, H. R. and Klett, J. D.: Microphysics of Clouds and Precipitation, 2nd Edition, Kluwer Academic, Dordrecht, 954 pp., 1997.

Purdy, J. C., Austin, G. L., Seed, A. W. and Cluckie, I. D.: Radar evidence of orographic enhancement due to the seeder feeder mechanism, Meteorol. Appl., 12(3), 199–206, doi:10.1017/S1350482705001672, 2005.

Qu, Y., Khain, A., Phillips, V., Ilotoviz, E., Shpund, J., Patade, S. and Chen, B.: The Role of Ice Splintering on Microphysics of Deep Convective Clouds Forming Under Different Aerosol Conditions: Simulations Using the Model With Spectral Bin Microphysics, J. Geophys. Res. Atmos., 125(3), 1–23, doi:10.1029/2019JD031312, 2020.

Ramelli, F., Henneberger, J., David, R., Bühl, J., Radenz, M., Seifert, P., Wieder, J., Lauber, A., Pasquier, J., Engelmann, R., Mignani, C., Hervo, M. and Lohmann, U.: Microphysical investigation of the seeder and feeder region of an Alpine mixed-phase cloud, Atmos. Chem. Phys., 21, 6681–6706, doi:10.5194/acp-21-6681-2021, 2021.

Rangno, A. L. and Hobbs, P. V.: Ice particles in stratiform clouds in the Arctic and possible

mechanisms for the production of high ice concentrations, J. Geophys. Res. Atmos., 106(D14), 15065–15075, doi:10.1029/2000JD900286, 2001.

Rasmussen, R. M., Geresdi, I., Thompson, G., Manning, K. and Karplus, E.: Freezing drizzle formation in stably stratified layer clouds: The role of radiative cooling of cloud droplets, cloud condensation nuclei, and ice initiation, J. Atmos. Sci., 59(4), 837–860, doi:10.1175/1520-0469(2002)059<0837:FDFISS>2.0.CO;2, 2002.

Reinking, R. F., Snider, J. B. and Coen, J. L.: Influences of storm-embedded orographic gravity waves on cloud liquid water and precipitation, J. Appl. Meteorol., 39(6), 733–759, doi:10.1175/1520-0450(2000)039<0733:IOSEOG>2.0.CO;2, 2000.

Reisner, J., Rasmussen, R. M. and Bruintjes, R. T.: Explicit forecasting of supercooled liquid water in winter storms using the MM5 mesoscale model, Q. J. R. Meteorol. Soc., 124(548), 1071–1107, doi:10.1002/qj.49712454804, 1998.

Roe, G. H.: Orographic Precipitation, Annu. Rev. Earth Planet. Sci., 33, 645–671, doi:10.1146/annurev.earth.33.092203.122541, 2005.

Rogers, D. C. and Vali, G.: Ice Crystal Production by Mountain Surfaces, J. Clim. Appl. Meteorol., 26, 1152–1168, doi:10.1175/1520-0450(1987)026<1152:ICPBMS>2.0.CO;2, 1987.

Rotunno, R. and Houze, R. A.: Lessons on orographic precipitation from the Mesoscale Alpine Programme, Q. J. R. Meteorol. Soc., 133, 811–830, doi:10.1002/qj.67, 2007.

Schlenczek, O., J. P. Fugal, K. N. Bower, J. Crosier, M. J. Flynn, G. Lloyd, and S. Borrmann, 2014: Properties of pure ice clouds in an alpine environment. 14th Conf. on Cloud Physics, Boston, MA, Amer. Meteor. Soc. [Available online at https://ams.confex.com/ams/14CLOUD14ATRAD/webprogram/Manuscript/Paper250304/Schlenczek_et_al_2014_AMS_extended_abstract_klein.pdf.]

Schmidt, R. A.: Measuring particle size and snowfall intensity in drifting snow., Cold Reg. Sci. Technol., 9, 121–129, doi:10.1016/ 0165-232X(84)90004-1, 1984.

Schwarzenboeck, A., Shcherbakov, V., Lefevre, R., Gayet, J. F., Pointin, Y. and Duroure, C.: Indications for stellar-crystal fragmentation in Arctic clouds, Atmos. Res., 92(2), 220–228, doi:10.1016/j.atmosres.2008.10.002, 2009.

Sharma, V., Gerber, F., and Lehning, M.: Introducing CRYOWRF v1.0: Multiscale atmospheric flow simulations with advanced snow cover modelling, Geosci. Model Dev. Discuss., doi:10.5194/gmd-2021-231, in review, 2021.

Sotiropoulou, G., Sullivan, S., Savre, J., Lloyd, G., Lachlan-Cope, T., Ekman, A. M. L. and Nenes, A.: The impact of secondary ice production on Arctic stratocumulus, Atmos. Chem.

Phys., 20, 1301–1316, doi:10.5194/acp-20-1301-2020, 2020.

Sotiropoulou, G., Vignon, E., Young, G., Morrison, H., O'Shea, S. J., Lachlan-Cope, T., Berne, A. and Nenes, A.: Secondary ice production in summer clouds over the Antarctic coast: An underappreciated process in atmospheric models, Atmos. Chem. Phys., 21(2), 755–771, doi:10.5194/acp-21-755-2021, 2021a.

Sotiropoulou, G., Ickes, L., Nenes, A. and Ekman, A.: Ice multiplication from ice–ice collisions in the high Arctic: sensitivity to ice habit, rimed fraction, ice type and uncertainties in the numerical description of the process, Atmos. Chem. Phys., 21, 9741–9760, doi:10.5194/acp-21-9741-2021, 2021b.

Sullivan, S. C., Hoose, C., Kiselev, A., Leisner, T. and Nenes, A.: Initiation of secondary ice production in clouds, Atmos. Chem. Phys., 18(3), 1593–1610, doi:10.5194/acp-18-1593-2018, 2018a.

Sullivan, S. C., Barthlott, C., Crosier, J., Zhukov, I., Nenes, A. and Hoose, C.: The effect of secondary ice production parameterization on the simulation of a cold frontal rainband, Atmos. Chem. Phys., 18, 16461–16480, doi:10.5194/acp-18-16461-2018, 2018b.

Takahashi, T., Nagao, Y. and Kushiyama, Y.: Possible High Ice Particle Production during Graupel–Graupel Collisions, J. Atmos. Sci., 52, 4523–4527, 1995.

Thompson, G., Rasmussen, R. M. and Manning, K.: Explicit Forecasts of Winter Precipitation Using an Improved Bulk Microphysics Scheme. Part I: Description and Sensitivity Analysis, Mon. Weather Rev., 132, 519–542, doi:10.1175/1520-0493(2004)132<0519:EFOWPU>2.0.CO;2, 2004.

Vali, G., Leon, D. and Snider, J. R.: Ground-layer snow clouds, Q. J. R. Meteorol. Soc., 138(667), 1507–1525, doi:10.1002/qj.1882, 2012.

Vardiman, L.: The Generation of Secondary Ice Particles in Clouds by Crystal–Crystal Collision, J. Atmos. Sci., 35, 2168–2180, doi:10.1175/1520-0469(1978)035<2168:TGOSIP>2.0.CO;2, 1978.

Vignon, É., Alexander, S. P., DeMott, P. J., Sotiropoulou, G., Gerber, F., Hill, T. C. J., Marchand, R., Nenes, A. and Berne, A.: Challenging and Improving the Simulation of Mid-Level Mixed-Phase Clouds Over the High-Latitude Southern Ocean, J. Geophys. Res. Atmos., 126(7), 1–21, doi:10.1029/2020jd033490, 2021.

Vionnet, V., Guyomarc'h, G., Naaim Bouvet, F., Martin, E., Durand, Y., Bellot, H., Bel, C. and Puglièse, P.: Occurrence of blowing snow events at an alpine site over a 10-year period: Observations and modelling, Adv. Water Resour., 55, 53–63, doi:10.1016/j.advwatres.2012.05.004, 2013.

1353 Vionnet, V., Martin, E., Masson, V., Guyomarc'H, G., Naaim-Bouvet, F., Prokop, A., Durand,
1354      Y. and Lac, C.: Simulation of wind-induced snow transport and sublimation in alpine
1355      terrain using a fully coupled snowpack/atmosphere model, Cryosphere, 8(2), 395–415,
1356      doi:10.5194/tc-8-395-2014, 2014.

1357 Willmott, C. J., Robeson, S. M. and Matsuura, K.: A refined index of model performance, Int.
1358      J. Climatol., 32(13), 2088–2094, doi:10.1002/joc.2419, 2012.

1359 Xu, L., Russell, L. M., Somerville, R. C. J. and Quinn, P. K.: Frost flower aerosol effects on
1360      Arctic wintertime longwave cloud radiative forcing, J. Geophys. Res. Atmos., 118(23),
1361      13282–13291, doi:10.1002/2013JD020554, 2013.

1362 Yano, J. I. and Phillips, V. T. J.: Ice-Ice collisions: An Ice multiplication process in atmospheric
1363      clouds, J. Atmos. Sci., 68(2), 322–333, doi:10.1175/2010JAS3607.1, 2011.

1364 Yano, J. I., Phillips, V. T. J. and Kanawade, V.: Explosive ice multiplication by mechanical
1365      break-up in ice-ice collisions: A dynamical system-based study, Q. J. R. Meteorol. Soc.,
1366      142(695), 867–879, doi:10.1002/qj.2687, 2016.

1367 Young, G., Lachlan-Cope, T., O'Shea, S. J., Dearden, C., Listowski, C., Bower, K. N.,
1368      Choularton, T. W. and Gallagher, M. W.: Radiative Effects of Secondary Ice Enhancement
1369      in Coastal Antarctic Clouds, Geophys. Res. Lett., 46, 2312–2321,
1370      doi:10.1029/2018GL080551, 2019.

1371 Zhao, X. and Liu, X.: Global Importance of Secondary Ice Production, Geophys. Res. Lett.,
1372      doi:10.1029/2021GL092581, 2021a.

1373 Zhao, X. and Liu, X.: Relative importance and interactions of primary and secondary ice
1374      production in the Arctic mixed-phase clouds, Atmos. Chem. Phys. Discuss.,
1375      doi:10.5194/acp-2021-686, in review, 2021b.

1376 Zhao, X., Liu, X., Phillips, V. T. J. and Patade, S.: Impacts of secondary ice production on
1377      Arctic mixed-phase clouds based on ARM observations and CAM6 single-column model
1378      simulations, Atmos. Chem. Phys., 21(7), 5685–5703, doi:10.5194/acp-21-5685-2021,
1379      2021.